Investigation of complex impurity centers in zinc oxide

by

Abbas Nakhlband

B.Sc., Sharif University of Technology, 2015

Thesis Submitted in Partial Fulfillment of the
Requirements for the Degree of
Master of Science

in the
Department of Physics
Faculty of Science

SIMON FRASER UNIVERSITY
Spring 2021

Declaration of Committee

Name:	**Abbas Nakhlband**
Degree:	**Master of Science (Physics)**
Title:	**Investigation of complex impurity centers in zinc oxide**
Committee:	**Chair:** Malcolm Kennett Associate Professor, Physics
	Simon Watkins Supervisor Professor, Physics
	David Broun Committee Member Associate Professor, Physics
	Gary Leach Examiner Professor, Chemistry

Abstract

Zinc oxide is a potentially useful material in optoelectronics. It has a 3.3 eV direct bandgap which makes it a comparatively inexpensive candidate for replacing gallium nitride as a UV light emitter. Production of stable p-type ZnO is the biggest challenge for the introduction of this material to industry. Many attempts to produce stable p-type ZnO by doping single atom point defects have failed. The remaining dopant candidates are complex defects including two or more components. In this thesis, we mostly focus on the study of bound excitons corresponding to Li related defects. We show that the line at 3353.4 meV in the UV spectra of ZnO, previously assigned to tin, is a complex donor impurity including Sn and Li atoms. We performed annealing experiments, diffusing the Li content out of the lattice. The intensity of the 3353.4 meV line decreased as a result of annealing, which suggests the involvement of Li in this impurity. This process was reversed by the introduction of Li into the sample and the original intensity was restored. This was strong evidence of the involvement of Li in this impurity. We found a 0.4 eV $\pm$ 0.2eV activation energy for the ejection of Li from the complex using the annealing results. Density functional analysis of a complex consisting of Li and Sn in the nearest neighboring Zn sites results in much bigger activation energies for different mechanisms of ejection of Li. This evidence suggests that the impurity is more complicated than Li and Sn in nearest neighboring Zn sites. We tried to further investigate this impurity by introducing a different isotope of Li. Substitution of natural Li (96% ^{7}Li) with ^{6}Li showed a change of -0.022$\pm$0.008 in the energy position of the recombination energy of the D^0X attributed to the line at 3353.4 eV. Our theoretical prediction of the shift suggested a lower limit of -0.031 for the expected shift.
In addition, we observed new Li-related lines and showed they are due to bound excitons. We also investigated the effect of the environment in which Li doping is done on the emergence of these new lines.

Keywords: Zinc oxide, complex point defects, bound excitons, spectroscopy, lithium doping, tin doping, acceptors, photoluminescence, isotope shift

Dedication

I dedicate this thesis to Narges and Mohsen, my Sister and my best friend.

Acknowledgements

I would like to thank my supervisor, Dr. Simon Watkins, for all his guidance and support he gave me through my research at his lab. Also I am thankful to my former supervisory committee member, Prof. George Kirczenow, for his advice and discussions in and out of my committee meetings, and to Prof. David Broun for taking over as supervisory committee due to Prof. Kirczenow's retirement. I want to thank all my lab-mates for their support during my education at SFU. I am grateful to the faculty and staff of Physics department, especially Rose Evans who always facilitated all the processes and contributed to greatness of the research environment here.

Table of Contents

List of Tables

List of Figures

Chapter 1

Introduction

Zinc oxide is a direct wide-bandgap semiconductor that belongs to the II-VI semiconductor system. Among its useful properties are high transparency in the visible region, and room temperature luminescence in the ultraviolet region. Reports on p-type conductivity and several other properties in this natively n-type semiconductor triggered an enormous increase in the number of papers published on ZnO since 1990 [1]. Nonetheless, stable p-type ZnO, which would make this material widely useful in optoelectronics, has not been developed yet. Among the biggest motivations that are pushing research on ZnO is the light-emitting capabilities that make it an ideal replacement for GaN which is considerably more expensive. Other potential uses of this material are applications in liquid crystal displays, energy-saving or heat-protecting windows and solar cells [1]. In addition, the exciton binding energy of 60 meV for ZnO [2] versus 25 meV for GaN [3] makes it a better candidate for some applications. Recently possible application in quantum information has been discussed using donor spins as qubits [4]. A better understanding of the defect structures and their effects on the conductivity of the material is crucial for controlling the conductivity in ZnO. There are very few reports of the identification of multi-atom defects in ZnO, despite the enormous technological interest. Lithium has been of high interest for p-doping of ZnO. In this thesis we will investigate the role of Li in a particular donor defect previously known to contain Sn. Using photoluminescence spectroscopy (PL), involvement of Li in this defect was confirmed by means of out-diffusion and in-diffusion experiments. Then we compared the activation energy of these processes we inferred from the experiment with the DFT calculations by our colleague, Manu Hegde. We attempted to further prove the involvement of Li in this defect by careful substitution of Li isotopes ^{6}Li and ^{7}Li. In addition we will report the observation of a whole new series of photoluminescence emissions, emerging as a result of in-diffusion of Li. We will prove the excitonic origin of these lines.

1.1 Luminescence Processes

Most of the investigations of the defects in this research are based on photoluminescence (PL) measurements. PL is the result of the transition of optically excited electrons, holes, etc. back to their ground states with lower energy. As a result of this transition a photon is emitted with energy $h\nu$ equal to the difference between the energy of the initial and the final state. Fig. 1.1 shows a schematic of a transition of a free electron from the conduction band to the valence band. In this example the photon energy is equal to the bandgap E_g. Some of the most common PL processes that are used in this research are explained in the following sections. The details of the experimental setup is explained in section 2.3.

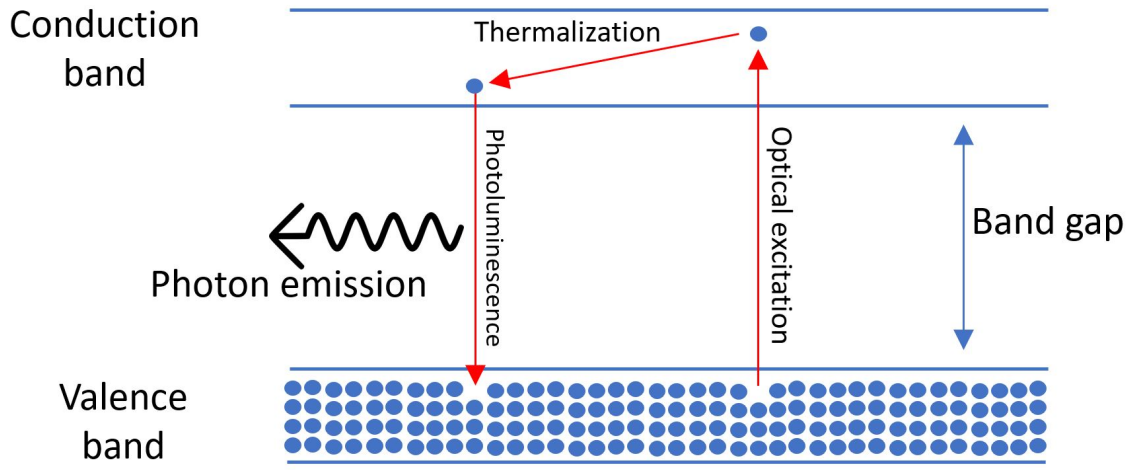

Figure 1.1: Schematic of an optical transition, illustrating emission of a photon by transition of free electron from the conduction band to an empty level in the valence band.

1.1.1 Free excitons(FX) and effective mass approximation

If an electron in the valence band becomes excited to the conduction band it leaves a hole in the valence band. A hole is the absence of an electron in an otherwise filled band that behaves like a positive charge. As a result, a free electron and a free hole can bind to each other at low temperature via the Coulomb force to form a bound state in a hydrogenic structure called a free exciton (FX). To form the Hamiltonian of an exciton we need to consider the difference between the behavior of the charges in a solid and vacuum. In this regard, we need to consider the dielectric constant of the solid and use the effective mass approximation (EMA). An electron or a hole in a solid reacts to an external force with an "effective mass", different from the electron mass in vacuum. This mass can be found based on the curvature of the bands at their minimum and maximum [5]:

$$\frac{1}{m^*} = \frac{1}{\hbar^2}\frac{\partial^2 E}{\partial k^2}[6], \tag{1.1}$$

In addition, we need to consider the effect of the screening of the valence band electrons in the solid. As a result of this screening, we can consider a greater permittivity $\epsilon_0\epsilon$ for the environment than the vacuum permittivity ϵ_0.

Eq 1.2 and eq 1.3 compares the Hamiltonian for an electron in a hydrogen atom with an exciton in a solid respectively:

$$\hat{H_H} = -\frac{\hbar^2}{2m_e}\nabla^2 - \frac{e^2}{4\pi\epsilon_0 r} \tag{1.2}$$

$$\hat{H_{ex}} = -\frac{\hbar^2}{2\mu^*}\nabla^2 - \frac{e^2}{4\pi\epsilon_0\epsilon r}, \tag{1.3}$$

where

$$\mu^* = \left[(m_e^*)^{-1} + (m_h^*)^{-1}\right]^{-1},$$

is the reduced mass of the electron and hole effective masses, m_e is the mass of electron, m_e^*=0.28m_e and m_h^*=0.59m_e [7] are the reduced masses of the electron and hole respectively and ϵ=8.75 [8] is the dielectric constant of the semiconductor. r is the distance between the positive and the negative charge in both equations. It is worth noting that for the hydrogen atom the motion of the proton had been ignored and it is assumed to be fixed, since its mass is very large. In contrast, for the exciton the electron and the hole are free in the lattice. A free exciton can have translational motion, therefore can have kinetic energy, which is ignored in the Hamiltonian.

By respective substitution of μ^* and $\epsilon_0\epsilon$ with m_e and ϵ_0 the Hamiltonian of the hydrogen atom transforms into the Hamiltonian of an exciton with zero kinetic energy. Thus, it is possible to estimate the Bohr radius and the binding energy of a FX using the effective mass approximation.

For the Bohr radius of the hydrogen atom we have $a_H = 4\pi\epsilon_0\hbar^2/e^2m_e = 0.53$Å. Performing the necessary substitutions, for the Bohr radius of an exciton we have:

$$a_{FX} = a_{\mathrm{H}}\frac{\epsilon}{(\mu^*/m_{\mathrm{e}})} = 2.4\mathrm{nm} \tag{1.4}$$

For the energy levels of an electron in a hydrogen atom we have $E_n = -\frac{e^4 m_{\mathrm{e}}}{32\pi^2\epsilon_0^2\hbar^2}\frac{1}{n^2}$. $n = 1$ gives the binding energy of $R_y = -13.6$ eV. Again, performing the necessary substitutions for the exciton binding energy, we have:

$$R_{ex}^* = R_y\frac{(\mu^*/m_{\mathrm{e}})}{\epsilon^2}. \tag{1.5}$$

ZnO has a 60 meV exciton binding energy [9]. This is a very large binding energy for an exciton in a semiconductor which makes it possible to observe them at room temperature. As a result of radiative recombination of an exciton, a photon is emitted. The minimum emission is equal to the bandgap energy E_g minus the exciton binding energy. As no impurity is involved in this process, it is called intrinsic luminescence, in contrast to the rest of the luminescence processes discussed later which are all due to involvement of some kind of impurity or defect.

1.1.2 Bound excitons (BX)

A bound exciton is formed as a result of an exciton binding to an impurity in the solid. An impurity with a different number of electrons in its outer shell than the atom it substitutes can contribute to the conductivity of the semiconductor. For example group III impurities, like Al, Ga and In located on a Zn site have one extra electron than Zn (group II) in their outer shell. This electron occupies an energy position close to the conduction band. At room temperature, this electron can become excited to the conduction band and increase the number of free electrons. Such impurities are called donors. Similarly, if an atom has fewer electrons in its outer shell than the atom it has substituted, it can borrow one from the core which leaves a hole (absence of electron) in its core. This hole contributes to the conductivity like a positive charge since the valence band is not full anymore, similar to the conduction band. These impurities are called acceptors.

As discussed in the previous section a free exciton is a hydrogenic structure consisting of an electron bound to a hole. A similar structure can be imagined for a donor in a solid. The extra electron of the donor sees the ion as a positively charged core. Eq (1.3), (1.4) and (1.5) apply to a donor as well, except that μ_h^* should be replaced with m_e^*. Similar to the hydrogen atom, a donor has a very heavy core with negligible motion relative to the center of mass. A free exciton can become bound to a neutral donor in a manner similar to the binding of two hydrogen atoms. In this situation the two electrons occupy a 1s orbital and act to bind the positive hole to the positive donor core. The top left structure in Fig 1.2 shows a schematic of the electron cloud, hole cloud, and the donor core in a neutral donor bound exciton (D^0X).

Similarly, an exciton and an acceptor can bind to form a neutral acceptor bound exciton (A^0X). By switching the roles of the electron and the hole, the Hamiltonian is similar. In this situation the hole of the exciton and the hole in the acceptor are in the acceptor 1s orbitals and are shared, resulting in a binding between the negative ion core and the electron of the exciton.

The localization of the exciton due to binding to a donor increases the exciton binding energy, and therefore the recombination energy of the exciton appears at a lower energy relative to the free exciton. The energy separation of a free exciton and a particular bound exciton is defined as their localization energy and it varies for different impurities [7]. In ZnO we observed exciton localization energies ranging from around 11 meV to 23 meV [7]. Bound exciton lines are significantly sharper than the FX lines since free excitons can have kinetic energy which widens the range of energies they can have. In contrast bound exciton emission is similar to atomic emission in that the electron and hole are bound to a particular lattice location.

Excitons may also be bound to ionized donors/acceptors. The resulting outcome is anal-

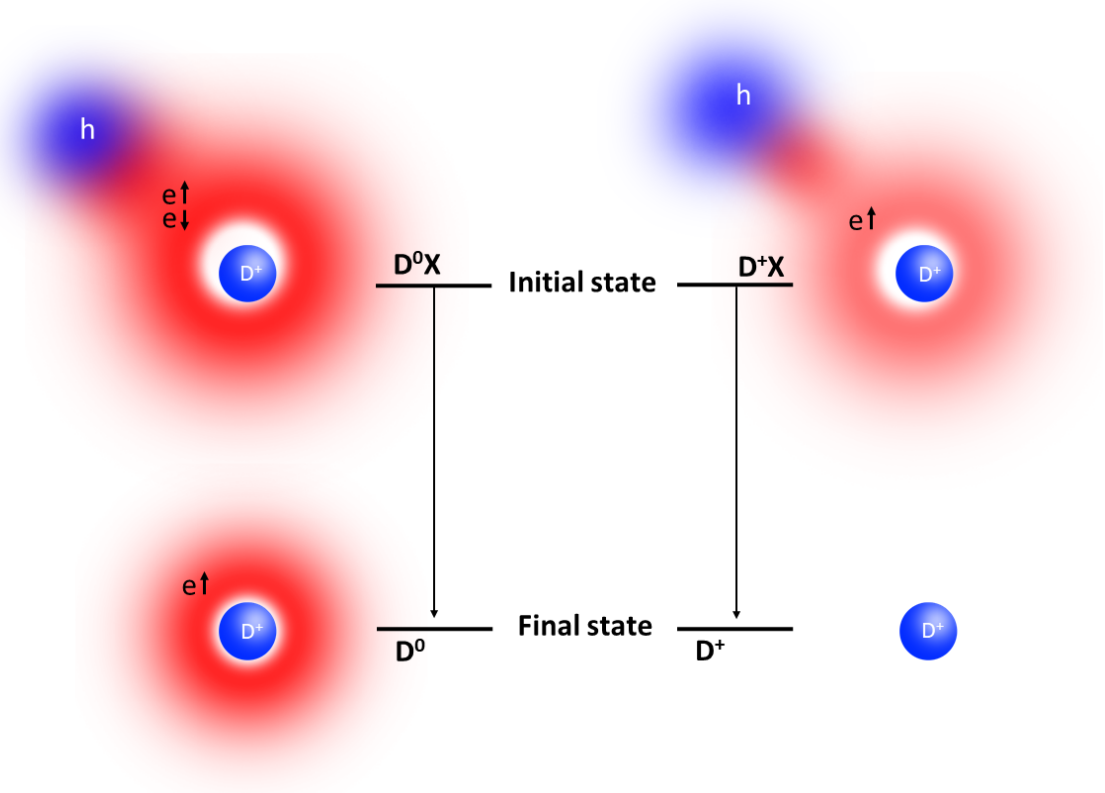

Figure 1.2: Schematic figure illustrating the arrangement of electron and hole around a donor defect before and after their recombination.

ogous to an ionized H_2 atom. This structure is called an ionized donor/acceptor bound exciton (D^+X/A^+X). In the case of a D^+X, there is only one electron shared with two positive charges, hence there is a lower electron cloud density around the positive charges compared to a D^0X, as indicated in Fig. 1.2. While positive charges repel each other, a binding occurs as a result of the screening by the electron cloud. Since the cloud of the D^+X is less dense and effective than the D^0X, the binding is weaker. We observed ionized

donor bound excitons in the PL spectra with localization energies around 5 meV to 10 meV. The appearance of ionized donor/acceptor bound excitons is likely due to compensation by deeper acceptors/donors.

Bound exciton lines in ZnO were studied by Reynolds et al. in 1965 [10]. Although many of the identifications of these lines were incorrect, the labeling they established stays in the literature until now. They called them I-lines and labeled ten of the widely observed lines from I_1 to I_{10}. Around 2002 to 2007 several of the lower energy emission lines were attributed to acceptor bound excitons (A^0X) such as Li[11], N[12], etc[13]. A very detailed and reliable review of these lines was done by Meyer et al. [7]. With strong evidence he assigned some of the lines to specific group III elements and hydrogen donors. All of the remaining I-lines were shown to be due to D^0X and not A^0X defects. Several of the I-lines we see in our samples are reported in his study including D^0X emission at substitutional Al, Ga, and In donors on Zn sites.

1.1.3 Two-electron-satellite (TES) lines

After recombination of a bound exciton the donor electron can end up in its ground state or in one of its excited states. As a result of the latter, the emission of the transition will have less energy than the original exciton recombination, which gives rise to new lines called two electron satellites (TES). Fig 1.3 shows a schematic diagram of the TES transitions with 1s and 2p donor final states. It should be noted that the 2p state is not necessarily above the 2s state. For a purely Coulombic potential, the 2s and 2p energies are degenerate (as in the H atom). In addition in section 4.2, we will see situations where 2s level is above the 2p.

The separation between the original D^0X line and the TES line is basically the energy separation between the final states of the transitions i.e. 1s level of the donor for a D^0X recombination and the excited state of the donor for a TES transition.
Based on the effective mass approximation similar to eq (1.5) for the donor binding energy we have:

$$R_d^* = Ry \cdot \frac{m_e^*}{m_e} \frac{1}{\varepsilon^2}, \tag{1.6}$$

where the only difference compared with eq (1.5) is the substitution of μ^* with m_e^*, since the mass of the positive charge is large and can be neglected in eq (1.4). Assuming the values m_e^*=0.28m_e and [7] and ϵ=8.75 [8], eq (1.6) yields the value of 50.10 meV for the donor binding energy. Correcting for the effect of the anisotropy and the polar interaction with optical phonons the value of 50.15 meV has been calculated [7]. However, in reality both larger and smaller binding energies have been measured due to the fact that EMA does not work perfectly close to the donor impurity where electron screening is altered due to the de-

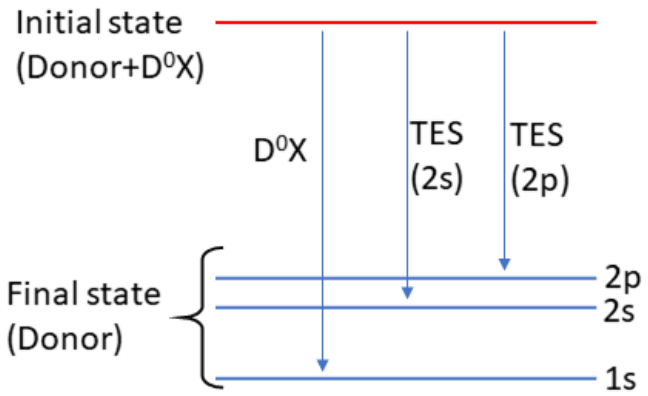

Figure 1.3: TES transition with the donor final state at 2s and 2p. The scales in this diagram are exaggerated. In reality the 2p-2s separation is very small compared to the 2p-1s.

tails of the core electron density. This is usually modeled by defining a short range "central cell potential" in addition to the Coulombic potential, which can increase or decrease the donor binding energy. In cases where the central cell potential is small the defect is usually called "shallow".

We can obtain an estimate of the donor binding energy from the spectroscopic data using

$$E_D = (E_{2p} - E_{1s}) + 12.6\ meV, \tag{1.7}$$

where $E_{2p} - E_{1s}$ is the measured separation between the D^0X principal transition and the 2p TES transition. 12.6 meV is the EMA value for the energy difference between the ionization level of the donor and the 2p state. This quantity is the same for all shallow donors assuming effective mass approximation predictions to be true further away from the impurity. This is sufficiently correct for the 2p orbital of a shallow donor since it has a node at the origin so that the central cell potential of the core is not seen by the electron.

1.2 Haynes' rule

Based on Haynes 1960 paper[14], the localization energy of an exciton at a point defect often has a linear relation with the donor or the acceptor binding energy of the impurity. Fig. 1.4 shows this linear relation for three of the group III single donors in ZnO.

As discussed in section 1.1.3, donor binding energies typically show small deviations from the effective mass approximation (EMA) due to the presence of the central cell potential. If the central cell potential is attractive the electron cloud in Fig 1.2 becomes closer to the

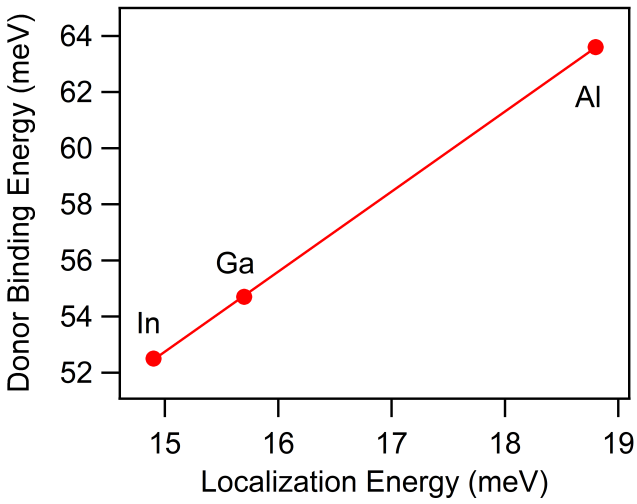

Figure 1.4: Haynes rule for group III single donor elements (In, Ga,Al) on Zn lattice site in ZnO. The horizontal axis shows the localization energy of the exciton at the impurity and the vertical axis shows the binding energy of the electron to the donor. In the literature, the axes are used in the opposite way, but for a better demonstration of our data in chapter 3, we chose to show them this way.

core and more dense. As a result the bound exciton which is sharing the electron cloud would be closer to the core as well and subsequently the binding between the exciton and the donor, localization energy, would be stronger. This qualitatively explains why the BX localization versus the donor binding energy is ascending but the linear relation remains empirical.

This linear relation between the localization energy of excitons and the donor binding energies is different for various semiconductors and also for BX lines with different structures in the same semiconductor. If the optical luminescence of a series of defects follows the rule, it reveals information about the electronic structure of the defects.

Based on the discussion in section 1.1.3 the difference between the 2p level and the donor ionization level is predicted to be constant at 12.6 meV for the shallow donors. Therefore Haynes rule predicts that $E_{2p} - E_{1s}$ will have a linear relation with the localization energy of the D^0X as well.

1.3 Density functional theory (DFT) and formation energy of defects

Density functional theory (DFT) is a computational method for calculating the electronic properties of quantum mechanical many-body systems. In this thesis we use the results of

DFT calculations performed by postdoctoral fellow Manu Hegde to investigate the formation energy and transition energies of the Sn-Li defect in ZnO. In 1964 Pierre Hohenberg and Walter Kohn showed that all the useful information about the electronic properties of a system, including the molecular geometry, bond energy, barrier heights, etc, can be derived from the electron density $n(r)$ of the system as a whole, rather than the wave function of the individual electrons[15]. This result, which is now called the Hohenberg-Kohn theorem, is the most important building block of the DFT method.

The Hohenberg-Kohn theorem states that in principal, a functional $F[n]$ for the energy of a system exists for any external potential. A functional is a function of a function. The ground-state electron density of the system is the $n_0(r)$ that minimizes this functional. $F[n]$ is independent of the many-body system under study, therefore, it is usually called the universal functional. It is worth noting, that the external potential includes the nuclei potentials, which are considered to be fixed cores using the Born-Oppenheimer approximation. The Hohenberg-Kohn theorem states that the wave-function of a many-body system is a functional of the electron density. Therefore, given the electron density, any observable can be calculated by being averaged by the wave function derived from the electron density. It is important to notice that the Hohenberg-Kohn theorem does not provide us with $F[n]$, which is the key to do actual calculations.

In 1965, the year after the Hohenberg and Kohn paper, Kohn and Sham published a paper in which they took a major step toward using the Hohenberg-Kohn theory for actual quantum mechanical calculations for real systems[16]. They broke the many-electron problem into many one-electron problems in an external potential caused by the positive core charges and the other electrons in the system. This method is basically an approximation that simplifies the problem. They introduced the Kohn-Sham equations[17]:

$$\left[-\frac{\hbar}{2m}\nabla^2 + V_{\text{ext}}(\boldsymbol{r}) + V_{\text{e}}(\mathbf{r}) + \mathrm{V_{XC}}(\mathbf{r})\right]\psi_i^{KS}(\boldsymbol{r}) = \epsilon_i(\boldsymbol{r})\psi_i^{KS}, \tag{1.8}$$

where ψ_i^{KS} are the single electron non-interacting wave functions (KS stands for Kohn-Sham [17]), $-\frac{\hbar}{2m}\nabla^2$ represents the kinetic energy, $V_{\text{ext}}(\boldsymbol{r})$ is the Coulombic potential of the atom cores, V_{e} the Coulombic interaction with the electron density and $\mathrm{V_{XC}}$ is the term that includes all the exchange-correlation energies that guarantees the Pauli exclusion principle and also compensates for the electron-electron direct interaction. It is worth noting that the term V_{e} includes part of the electron-electron interaction but in an average way using the mean-field approximation [17]. To correct the approximation for the exact equation the rest of the electron-electron interactions are embedded in the exchange-correlation term.

V_{e} is dependent on the electron density which is unknown before solving the Kohn-Sham

equations. Therefore in the DFT method they start with the best guess for the total electron density of the system. Solving the Kohn-Sham equations gives the individual wave functions ψ_i^{KS}. Then a more accurate electron density can be derived using:

$$n(\mathbf{r}) = \sum_{i}^{N} \left|\psi_i^{KS}(\mathbf{r})\right|^2. \tag{1.9}$$

This electron density can be used for finding a more accurate V_{e} and subsequently more accurate ψ_i^{KS}. After multiple iterations, if the final electron density was the same as the initial density the iteration will stop. All of the other needed quantities can be calculated using the final ψ_i^{KS} and electron density. For example for the energy of the system we have:

$$E\left[\{\psi_i\}\right] = -\frac{h}{m_e}\sum_i \int \psi_i^s \nabla^2 \psi_i d^3r + \int V(r)n(r)d^3r + \frac{e^2}{2}\iint \frac{n(r)n\left(r'\right)}{r-r'} d^3r d^3r' + E_{XC}[\{\psi_i\}][17]. \tag{1.10}$$

The first term on the right side of this equation is the kinetic energy, the second term is the electron-nuclei interaction, the third term is the mean-field electron-electron interaction and E_{XC} is the exchange-correlation functional.

At this point if the nuclei are not at equilibrium their positions are adjusted so the force on them $\mathbf{F} = -\nabla E(\mathbf{R})$ is relaxed. After multiple iterations when the adjustment of the nuclei positions converges to zero the resultant electron density is the final result from which all the properties of the structure can be derived. Fig. 1.5 shows a flowchart summary of the DFT method [17].

To further reduce the number of variables, the frozen core approximation is used. Based on this approximation, the core electrons are considered as a whole with no internal dynamics to simplify the dynamics of the system. This is the basis of the pseudo-potential method. The outer shell electrons are under the influence of the whole core which consists of the nuclei and the core electrons. Using a variety of pseudopotentials classified in libraries the core potential is estimated.

Kohn proved that $\mathrm{V_{XC}}$ or $\mathrm{E_{XC}}$ exists but we do not exactly know what this functional should be for the desired system. Therefore, it has to be approximated. Finding better approximations for the exchange-correlation terms is an ongoing field. However, many methods for approximating V_{XC} and E_{XC} have been developed [18], which are beyond the scope of this section.

The scale of the simulation depends on the unit cell one implements, called the supercell. The interactions across a supercell to the unit-cell adjacent to it are considered by

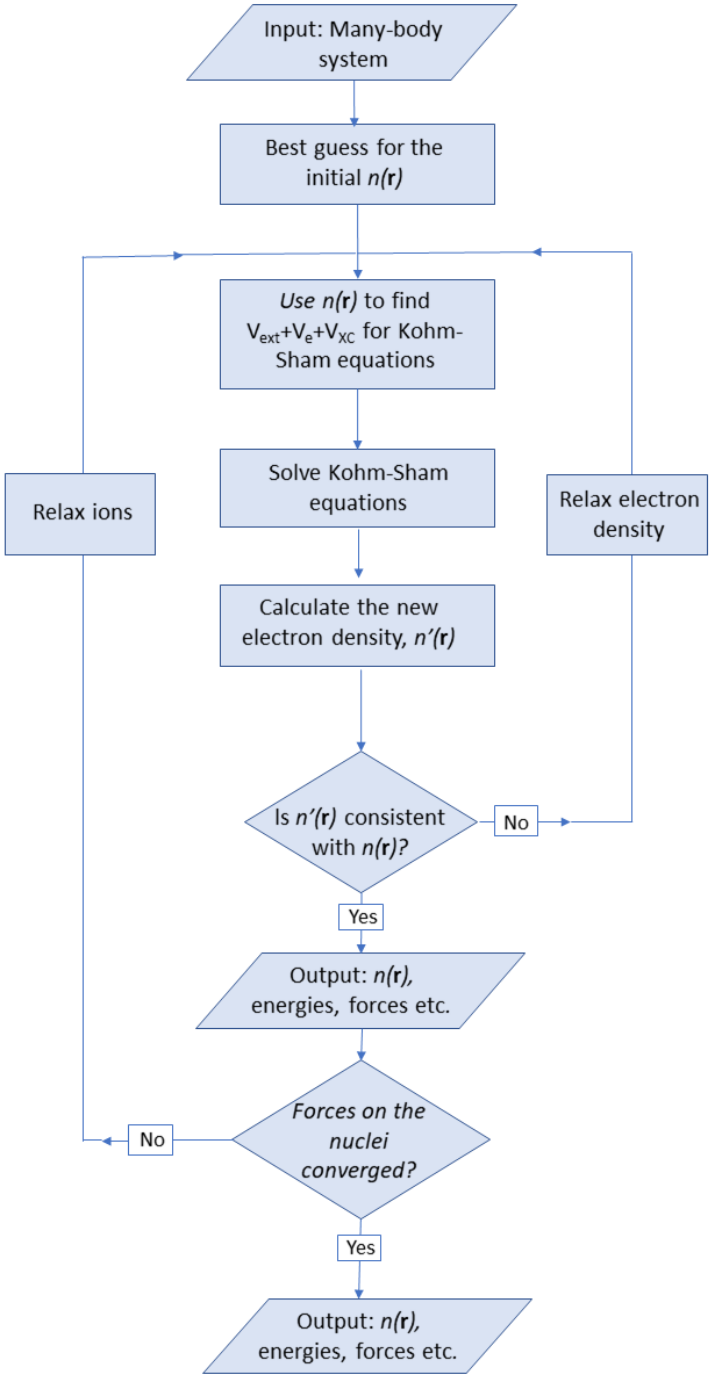

Figure 1.5: A summary scheme of the DFT method based on the reference [17].

forcing periodic boundary conditions to the simulation. While a smaller unit-cell makes the simulation easier and faster, there is a limitation to how small it can be. The supercell needs to be large enough to isolate the long-range interactions. For example, electron-defect interactions. This is why in cases of very long-range effects, DFT cannot be useful, as the simulation time grows exponentially with the supercell size.

In this work, the DFT method has been used by postdoc Manu Hegde in the Watkins group to calculate the formation energy of the defects. During the process of formation of a defect from the pure lattice, the pressure and the temperature of the environment is not assumed to change, hence it is an isothermal-isobaric process. Therefore the energy required to form the defect is given by the Gibb's free energy of formation ΔG_f [19]. The Gibb's free energy is defined as:

$$\begin{aligned} G(p,T) &= U + pV - TS \\ G(p,T) &= H - TS \end{aligned} \tag{1.11}$$

where p and T are pressure and volume, T and S are temperature and entropy U and H are internal energy and enthalpy respectively. In a solid we have[19]:

$$G = E^{\text{el}} + E^{\text{vib}} - TS^{\text{vib}} + pV \tag{1.12}$$

where indices E^{el} and E^{vib} stand for electronic and vibrational contributions to the internal energy, respectively and S^{vib} is the vibrational entropy. At moderate temperatures and pressures, i.e. room temperature and atmospheric pressure, the vibrational terms and pV are small. Thus, within a certain accuracy the total energy derived from a DFT simulation can represent the Gibb's energy ($G \approx E^{\text{el}}$) [19], which enables one to calculate the formation energy.

In general for the formation energy we have:

$$E_f^q\left(D, E_F\right) = E_{tot}^q(D) - E_{bulk} - \sum_X n_X \mu_X + q\left(E_F + E_v\right), \tag{1.13}$$

where $E_f^q\left(D, E_F\right)$ is the formation energy of the defect D in a material with the Fermi energy of E_F, q is the charge of the defect, E_{tot}^q is the total energy of the supercell with the defect in it, E_{bulk} is the total energy of the pure supercell, n_X is the number of the elements of kind X in the defect, μ_X is the chemical potential of the element and E_v is the energy of the maxima of the valence-band.

The environment can affect the amount of energy that the addition of a particular element to the system will cost i.e. the chemical energy. Let's consider the case of a Ga impurity substituting for Zn sites in ZnO. The higher the concentration of Ga in the environment,

the lower the formation energy of a Ga_{Zn} is. This decrease in the formation energy can be explained by an increase in the chemical potential of Ga [see Eq. (1.13)]. In addition, if a defect has a charge, the Fermi level (E_F) directly affects the formation energy since E_F is the energy that the added charge will possess.

It is worth noting that the relation between the formation energy and the Fermi level is linear with the slope being the charge of the defect. Later in this research, we will show DFT results showing the plots of the formation energy of the defects versus the Fermi level.

One can find the charge transition levels of the defect from charge state q to q' from the intersection of the E_f^q and $E_f^{q'}$ versus Fermi energy plot. Fig 1.6 shows an example of $E_f^{q=1+}$ and $E_f^{q=0}$ versus Fermi energy. The solid lines show the most stable charge state i.e. the one with the lowest formation energy. If we define $\epsilon(q/q')$ as the transition energy level from q to q' we have[20]:

$$\varepsilon\left(q/q'\right) = \frac{E_f\left(D^q; E_F = 0\right) - E_f\left(D^{q'}; E_F = 0\right)}{q' - q}, \tag{1.14}$$

This level is important because it determines at what energy level the carrier donation happens. If it is close to the band gap that means the defect is a shallow donor or deep acceptor and vice versa.

1.3.1 Model of isotope shift in the recombination energy of D^0X

In this section, we are going to discuss a model that provides an estimation of the shift in the energy of electronic transitions of a defect as a result of isotope substitution of its components. This model is based on a paper by V. Heine et. al. [21] The discussion begins by assuming that the defect is an independent Einstein oscillator with distinct electronic states. The solid is initially assumed to be a one atom solid. Later in the paper, the model is refined to represent a two-atom solid, using the Debye model. Basically, we will discuss the total energy state of an impurity when a carrier (an electron a hole or both) is trapped on it, and compare this with the ground state of the impurity with no or negligible charge. The former will be referred to as the initial state and the latter will be the final state. The presence of charge on a defect is expected to cause a softening of the vibrational modes of the defect. In addition, a change in the mass of the impurity can affect those energy levels due to electron-phonon coupling. In the case where the dependence of the initial and the final energy levels on the impurity isotope and the charge on the defect does not cancel out, it will affect the transition energy between those levels, resulting in an isotope shift that can be observed in the PL measurements.
Let's say for the localized vibration of the impurity without the carrier we have $M\omega^2 = \Lambda$,

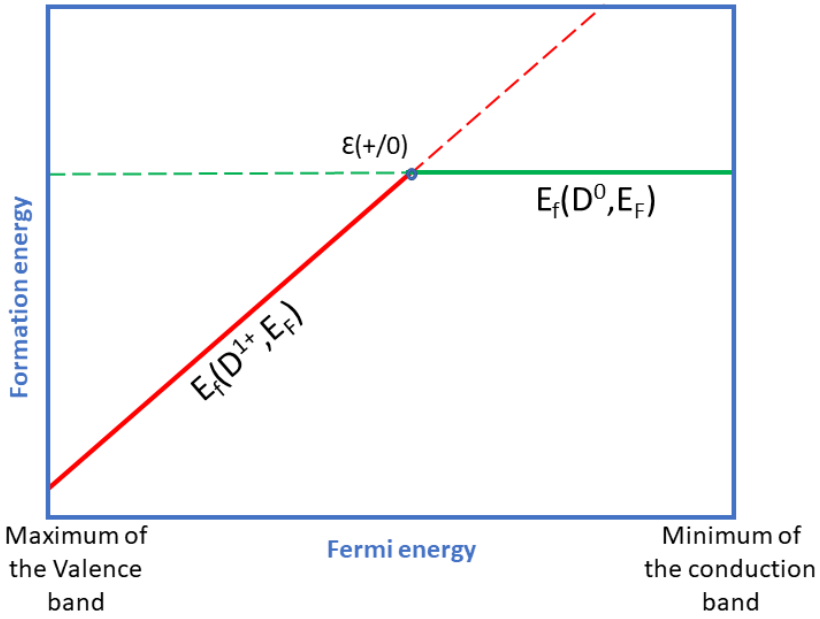

Figure 1.6: Formation energy as a function of the Fermi energy for a defect with two different charges. The solid line shows the minimum formation energy and the intersection of the two lines shows the transition energy from one charge to the other [17]. This figure demonstrates a deep donor situation since the intersection is far from the minimum of the conduction band.

where Λ is the force constant of the Einstein oscillator and M is the mass of the oscillator. The presence of a carrier softens the binding of the impurity with the neighboring atoms, and decreases the Λ. For an electron, the softening happens due to the extra screening between the two positive atom cores. Therefore we have:

$$M\omega^2 = \Lambda\left(1 - \gamma_c P\right), \tag{1.15}$$

where P is the probability of the presence of the trapped carrier on the oscillator i.e. in the space between the impurity and the nearest neighboring atoms. P is less than one because the wave function is delocalized. γ_c is the softening caused by a charge located on the oscillator. "c" stands for "carrier". A change in the isotope of the impurity changes its mass, let say as much as ΔM. For the altered isotope, we have

$$(M + \Delta M)(\omega + \Delta\omega)^2 = (\Lambda - \gamma_c P), \tag{1.16}$$

Expanding the equation to the first order we will have:

$$\omega^2 + 2\omega\Delta w = \frac{\Lambda}{M}\left(1 - \frac{\Delta M}{M}\right)(1 - \gamma_c P) \tag{1.17}$$
$$= \frac{\Lambda}{M}\left[1 - \gamma_c P - \frac{\Delta M}{M} + \gamma_c P\frac{\Delta M}{M}\right].$$

It is worth noting that this is a general equation for both the initial and the final state. For the final state with the carrier released from the trap its wave function is spread over the whole solid, therefore $P = 1/N$ will be negligible, where N is the number of atoms. This is in that the probability of finding the carriers at each atom in the solid is considered to be almost the same when the carrier is not trapped. After isolating the $\Delta\omega$ and multiplying by $\frac{\hbar}{2}$ and then 3 for three dimensions, for the shift in the zero-point energy of the oscillator we have:

$$\Delta E = \frac{3\hbar\Delta\omega}{2} = \frac{3\hbar}{4\omega}\left[-\gamma_c P - \frac{\Delta M}{M} + \gamma_c P\frac{\Delta M}{M}\right] \tag{1.18}$$

In this equation, there are three terms in the brackets causing a shift in E_0, hence the

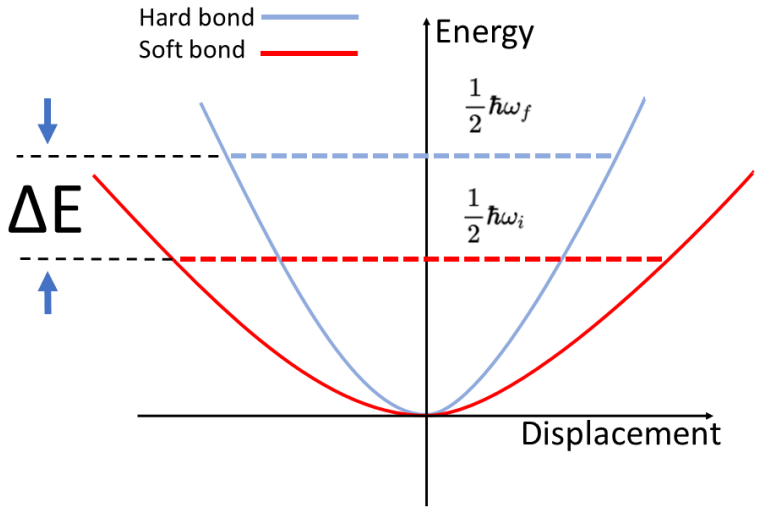

Figure 1.7: A schematic of the decrease in zero-point lattice vibration energy before and after softening of the atomic bonds, assuming a fixed mass.

energy of the states. Fig. 1.7 shows a schematic of the decrease in the energy level as a result of the softening of the atomic bonds. In the following, we discuss the effect of each one of the terms in the brackets on the optical transition from the initial state to the final state. From the left, we have $\gamma_c P$. This term is negligible for the final state as discussed. For the initial state P is considerably bigger than $P = 1/N$ as we discuss in the next section.

This term shows up in the transition energy, but it is the same for both isotopes. Therefore, although it affects the transition it does not distinguish the isotopes. Then we have $\frac{\Delta M}{M}$ which cancels out between the final state and the initial state for the altered isotope and thus does not affect the transition energy. Last, we have $\gamma_c P\frac{\Delta M}{M}$. This term is the one that results in an isotope shift since it affects the transition energy but only for the impurity with altered isotope. Depending on which isotope is taken as the original one $\frac{\Delta M}{M}$ can be positive or negative. For the isotope shift we have:

$$\begin{aligned} S = \Delta E_i - \Delta E_f &= \frac{3}{2}\hbar\Delta\omega \\ &= \frac{3}{4}\frac{\hbar}{\omega}\frac{\Lambda}{M}\frac{\Delta M}{M}\gamma_c P \\ &\approx \frac{3}{4}\hbar\omega\frac{\Delta M}{M}\gamma_c P \end{aligned} \tag{1.19}$$

Figure 1.8 shows a schematic of all the energy shifts and the isotope shift based on the Eq. (1.18). The purpose of this figure is to make the isotope shift (S) appear as clearly as possible. For this reason, part (b) of the figure is moved up so that the bottom of the transition arrows align. This is not a shift in energy as the blue dashed lines indicate.

The parameter γ_c is preventing us from directly calculating the shift as it is difficult to measure experimentally [21]. It is possible to relate γ_c to the temperature dependence of the bandgap of the host lattice. There are two contributions to the temperature dependence of the bandgap. One is due to the lattice expansion with increase of temperature, and the other is due to the mode softening caused by γ_c and the e-h pair produced as a result of electron excitation from valence band to the conduction band. Mode softening is responsible for 80 percent of the bandgap temperature dependence [21] [22] [23]. Therefore we can neglect the effect of lattice expansion by increase of temperature on the bandgap. A simple derivation can be given based on an Einstein model for the lattice [21]. In terms of the lattice vibrational energy we have:

$$E_g = E_g^0 + \sum_i \hbar\Delta\omega_i \left\langle n_i + \frac{1}{2}\right\rangle, \tag{1.20}$$

where E_g^0 is the band gap at zero temperature, n_i is the quantum number of the ith host lattice Einstein mode and $\Delta\omega$ is the softening of the ith mode due to the e-h charge. Taking the derivative and substituting $\langle n_i\rangle = kT/\hbar\omega_i$ ($kT \gg \hbar\omega_i$) one can show [21]:

$$\left(\frac{dE_g}{dk_B T}\right)_{\mathrm{HT}} = -3\gamma/2, \tag{1.21}$$

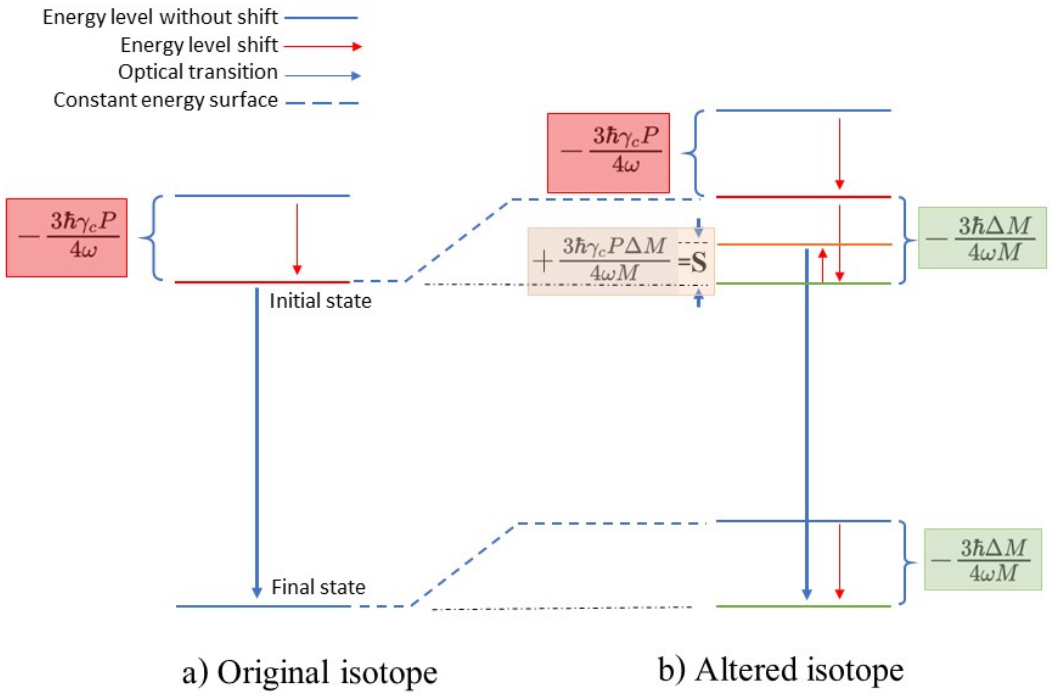

Figure 1.8: Shift in the energy of the states for the original isotope and the altered isotope as a result of bond softening and isotope. The terms on the figure can be found in Eq. (1.18). Terms shown with the same color are the same for better visualization. Note: The upward shift in part (b) of the figure is only for making S appear more clearly and does not represent an actual shift in the energies. The blue dashed line represent a constant energy level. a) The initial state shows a decrease in the energy level due to the softening of the bonds. This decrease shows up in the transition since the final state is not shifted. b) The altered isotope shows two decreases in the initial state. The first decrease is the same as for the original isotope. The second decrease, the green term due to the difference in mass compared to (a), does not affect the transition since it cancels out with a decrease in the final state of the altered isotope at the same amount. At last, we have an increase in the initial state of the altered isotope, a cross term that is due to both mass difference and softening, which shows up in the transition since does not exist in the final state. This shift also distinguishes the altered isotope from the original isotope since is only effects the altered isotope.

where γ is sum of the γ_h for a hole and γ_e for an electron and HT stands for high temperature. Assuming Λ for the impurity is the same as for the host atoms, ω is related to the host vibration frequency ω_0 by:

$$\omega = (M_0/M)^{1/2}\,\omega_0 \tag{1.22}$$

Substituting Eq. (1.22) in (1.19) and using (1.21) we have:

$$S = \frac{\hbar\omega_0}{2}\left(\frac{M_0}{M}\right)^{1/2}\frac{\Delta M}{M}\left(-\frac{dE_g}{dk_B T}\right)_{\mathrm{HT}}\frac{\gamma_c}{\gamma}P \tag{1.23}$$

Using Eq. (1.21) helps with experimental measurement of S since it brings the term $(\frac{\gamma_c}{\gamma})$ into the equation, which is less than 1 ($\gamma_e + \gamma_h = 1$), and is not expected to change the order of magnitude of S. Therefore an estimation of S becomes possible if we have P, since the term dE_g/dk_BT is an experimentally known quantity.

It is possible to derive a similar equation based on the Debye model and consider the solid as a two-atom material with an impurity atom siting on one of the sites[21], which is a better representation of an actual solid. It is worth mentioning that in our model for the defect under study we have two impurity atoms, Sn and Li, sitting on two nearest neighboring Zn sites. The Sn atom will not have any contribution to the isotope shift since its isotope does not change. Based on the Debye model for the isotope shift we have [21]:

$$S = \frac{2}{5} k\Theta_D \left(\frac{M_0}{M}\right)^{1/2} \frac{\Delta M}{M} \frac{\gamma_c}{\gamma} \left(-\frac{dE_g}{dkT}\right)_{\mathrm{HT}} P \tag{1.24}$$

where Θ_D is the Debye temperature, M is the mass of the element whose mass has altered and M_0 is the harmonic mean of the masses of the atoms in the solid. Assuming most of the solid is made of only two kinds of atoms, $N/2$ atoms of mass M_1 and $N/2$ of mass M_2 we have:

$$M_0^{-1} = \frac{1}{2}\left(M_1^{-1} + M_2^{-1}\right) \tag{1.25}$$

Eq (1.21), based on the Einstein model, restricts $\frac{dE_g}{dk_BT}$ to be a quantity between zero and -1.5, since $0 < \gamma < 1$ based on its definition. Utilizing the Debye model, this restriction does not exist [21].

We will not go into more details on the derivation of the model based on the Debye model as it has been thoroughly explained elsewhere [21].

Eq. (1.24) is an equation with all the parameters known from the experiment except for P, which we estimate in the next section.

Chapter 2

Experimental techniques

This chapter includes discussions on the equipment and the methods used in this research. Methods for the diffusion of impurities into the ZnO bulk samples are discussed and an overview of the photoluminescence (PL) system used to characterize the samples are presented.

2.1 Sample preparation using chemical vapor transport growth

Chemical vapor transport (CVT) is a method of growth that was used to synthesize our bulk crystal ZnO samples intentionally doped with Sn. The samples were synthesized at the Materials Science and Technology Division, Oak Ridge National Laboratory by the L.A. Boatner group. Experimental methods are briefly described in a previous paper by the Watkins lab [24]. In this process spheres made of a mixture of polycrystalline ZnO and 0.15 mol% of SnO_2 tube undergo a reaction with H_2(g) at 1250°C in an alumina tube. This reaction provides Zn in a gaseous form:

$$ZnO(s) + H_2(\ g) \rightarrow Zn(g) + H_2O(g) \tag{2.1}$$

Using nitrogen carrier gas the vapor is transported to the growth region at a lower temperature. In this region, a crystal grows via the reaction of the Zn(g) with oxygen:

$$Zn(g) + (1/2)O_2 \rightarrow ZnO(s) \tag{2.2}$$

In addition, the residual H_2 gas from the previous reaction turns to water vapor after reacting with O_2. A schematic of the setup is presented in Fig 2.1.

By this technique, ZnO crystal needles are produced with dimensions of 0.2-2 mm in diameter and a maximum length of 5 cm. Also, in some growths, large bulk crystals with more random shapes were produced.

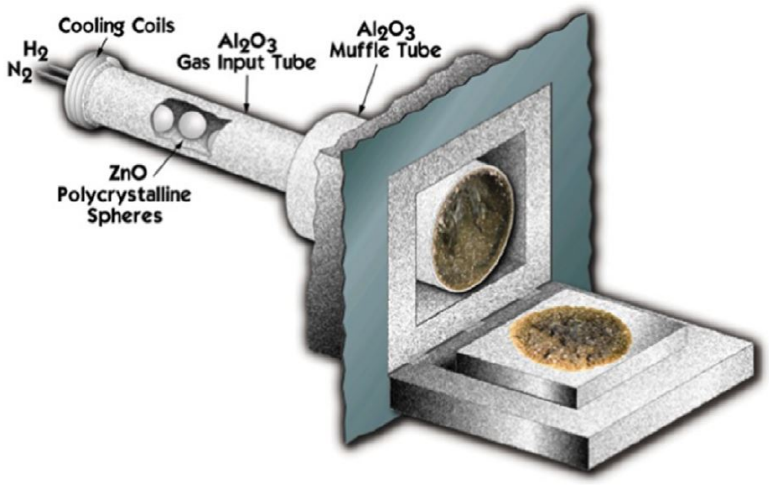

Figure 2.1: A schematic of the chemical vapor transport setup. [24].

A wide variation of the apparent Sn concentration in different runs was observed due to variation of the temperature at the growth region and other local growth condition variations. The concentration of Sn in the crystals was not directly measured. We used the intensity of the luminescence from a Sn related defect in the crystal as a rough indicator of the Sn concentration. Later in this thesis we will show that this defect called I_{10} is more than just an Sn impurity. Therefore this measurement is not very accurate.

2.2 Li diffusion

To diffuse Li atoms into the sample, initially, we added a lithium carbonate (Li_2CO_3) coating to the ZnO samples and then annealed them under N_2 or O_2 carrier gas. The diffusion was also carried out with Li_2CO_3 having two different isotope concentrations. We used enriched Li with 96% ^{6}Li and 4% ^{7}Li, or natural Li with 96%^{7}Li and 4% ^{6}Li.

2.2.1 Lithium carbonate coating

An oversaturated solution of water and lithium carbonate was prepared. Droplets of the solution were dropped on the surface of the samples. After water was evaporated from the solution, a layer of lithium carbonate remained on the sample. Fig.2.2 shows an optical microscope image of the surface of one of the samples before and after coating. Sometimes in order to make the process happen faster, we used a heater at a temperature below 60°C to vaporize the water.

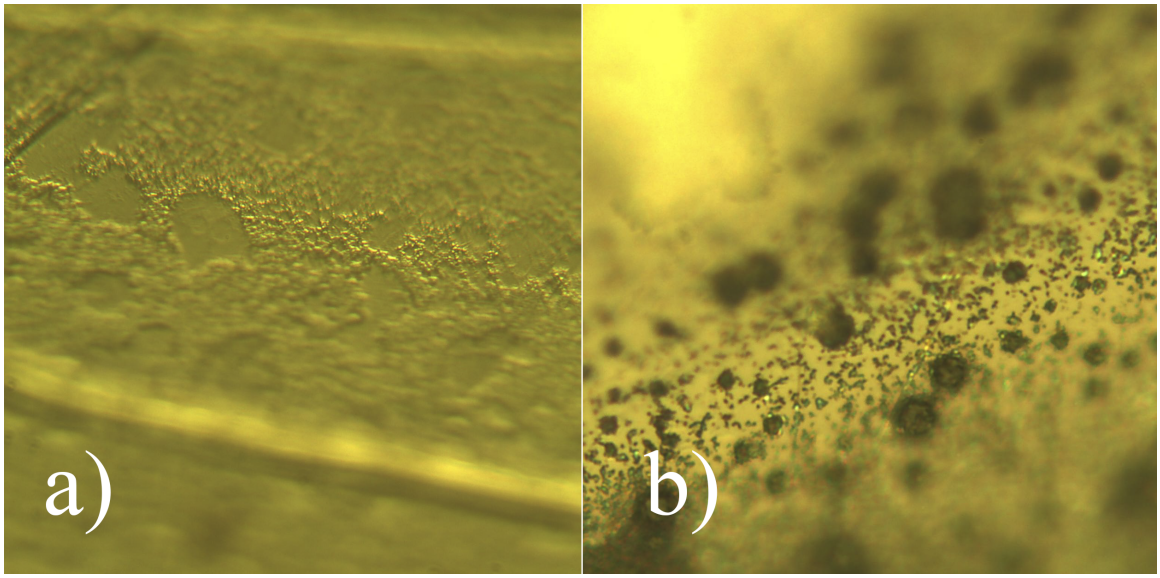

Figure 2.2: a) Optical microscope image of the surface of a ZnO bulk crystal. b) Optical microscope image of the surface of a ZnO bulk crystal coated with Li_2CO_3.

2.2.2 MOCVD reactor for annealing and isotope doping studies

To anneal the samples we used a metalorganic chemical vapor deposition (MOCVD) reactor. MOCVD is basically a thin film growth method. The main reason for using it for annealing rather than a regular furnace was to have accurate control over the contamination of the environment. A standard nanowire growth of our MOCVD system shows strong PL with lines due to known trace impurities. Fig. 2.3 (green curve) shows the standard grown PL with very low residual contamination. This guarantees that external contamination from the growth chamber will not have unpredictable effects on the PL of the annealed samples.

In addition, the use of the MOCVD reactor has another substantial advantage in isotope doping in avoidance of cross-contamination between the two isotopes of Li used for diffusion. In order to prevent cross-contamination, two separate sets of containers and pipettes were used for each solution of water and lithium isotope. The environment in which the sample was annealed was cleaned before changing the isotope of lithium for the next diffusion. The liner and the susceptor of the MOCVD reactor were initially cleaned in HCl/water(1:4) solution for about 24 hours and then baked. Finally, the MOCVD reactor was annealed at 950°C for 4 hours under a high flow of N_2 gas, 3 liters per minute. MOCVD has the advantage that we can confirm that Li contamination was removed by looking at the PL from a standard ZnO nanowire growth before and after cleaning. Li is a deep acceptor and reduces the PL luminescence of the sample tremendously due to compensation with the donors. Fig 2.3 shows the PL result of a standard nanowire run before and after cleaning the chamber. More than one order of magnitude decrease in the PL was observed as a re-

sult of the Li contamination. The final result after cleaning the chamber shows PL with an intensity comparable to the sample grown before Li diffusion. This confirms the removal of Li contamination from the MOCVD liner and susceptor.

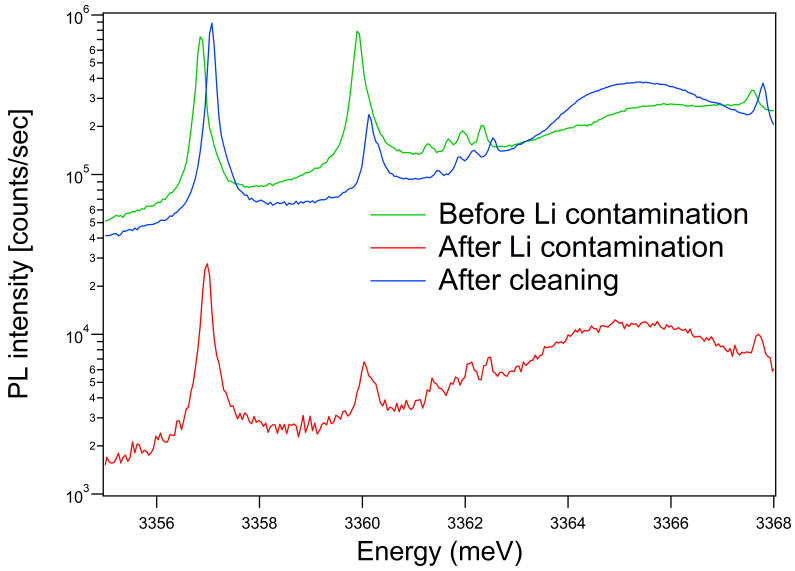

Figure 2.3: PL measurement for standard ZnO nanowire growth in MOCVD before and after Li contamination, and also after cleaning the chamber from the contamination

2.2.3 Removing the lithium carbonate coating

After the annealing in order to remove the lithium carbonate coating, we placed the sample in DI water and subjected the sample to ultrasound. We waited for 10 minutes before taking the sample out and rinsing it with isopropanol.

2.3 Photoluminescence

In a photoluminescence spectroscopy experiment, the ZnO sample is excited by a UV light source, a He-Cd laser in our case, with energy just above the bandgap to excite the electrons to the conduction band. As a result of thermalization at low temperatures the excited electron and the hole created in the valence band quickly bind together and create several forms of bound states discussed in the last chapter. The photons emitted as those bound states recombine are dispersed using a double spectrometer and detected by a photomultiplier. The number of photons emitted is recorded as a function of wavelength and energy.

Among the advantages of PL spectroscopy are: simplicity of setup, high sensitivity to low impurity concentrations and non-destructiveness.

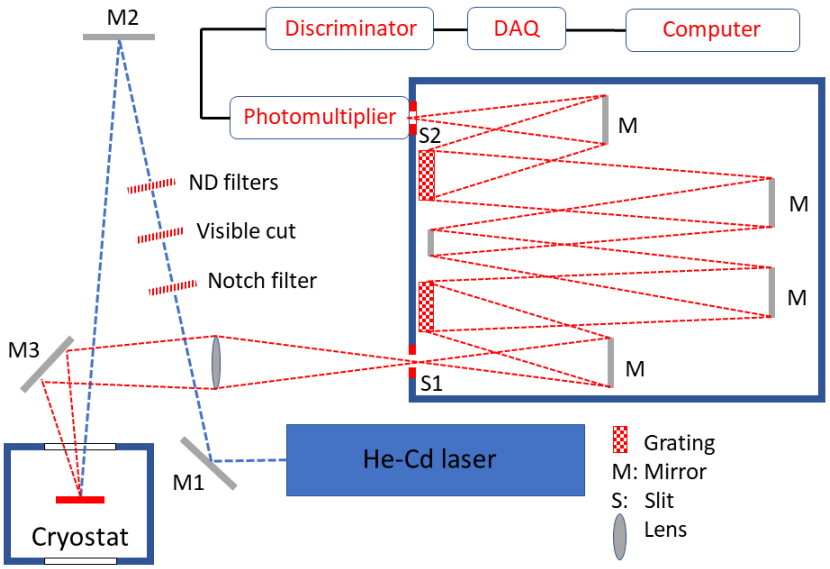

Figure 2.4: A schematic diagram of the PL spectroscopy setup at SFU.

A schematic diagram of the setup used for PL spectroscopy at SFU is shown in Fig. 2.4. The laser beam was aimed at the sample in the cryostat by mirrors 1 and 2. The emission from the sample was focused on the entrance slit of the double spectrometer (S1) after being reflected by the mirror 3. The beam was diffracted by the gratings twice and entered the photomultiplier from S2. A discriminator was used to remove the weak pulses that are not due to the detection of a photon, and the photon pulses to a standard digital format. The pulses are then counted by a National Instruments digital-analog acquisition device (DAQ) and recorded by a computer.

2.3.1 Light source

A He-Cd laser made by Kimmon Koha Co was used to excite the samples. This laser emits a 20 mW beam at 325nm(UV). The filters used in the setup are a narrow band interference filter (notch filter) and a visible cut filter. The aim is to block plasma lines from the laser. Two UV mirrors of diameter 25.4 mm (M1 and M2 in Fig. 2.4) were used to steer the laser beam to the sample. Emission from the sample was collected using a 75 mm $\times$ 75 mm aluminum mirror with high reflectivity at UV region and surface flatness of about one-quarter of the wavelength. In order to control the intensity hitting the sample, we used neutral density (ND) filters in our setup with attenuations of 10^{-1} to 10^{-4}. These filters were occasionally used when a reduction in the intensity of the pulse was needed in the middle of a PL scan. Just narrowing the slits would increase the resolution and the sharpness of the lines which usually was not desired in the middle of a scan.

It is worth mentioning the 325 nm wavelength has a very small penetration depth. The absorption coefficient of this wavelength in ZnO is about 1.6×10^5 cm^{-1} [25] which results in a 63 nm penetration depth.

2.3.2 Cryostat

A cryostat (Janis Corporation Varitemp) was used to bring the sample to a temperature of around 4.2 K. The sample was mounted on a copper block using teflon tape. The air in the dewar was substituted with helium gas to prevent the formation of frost on the sample. A combination of a heater and a silicon diode temperature sensor was able to maintain the temperature of the sample at any temperature above 4 K and below room temperature while the cryostat was running.

2.3.3 Grating spectrometer and photon counting

To monochromatize the collected luminescence from the sample a double spectrometer was used. The double spectrometer had a 0.85 m focal length and groove density of 1200 grooves/mm. A slit width of 20 μm was used for nearly all of our PL spectra, both for the incoming and outgoing beam.

To detect the outgoing beam it was sent to a Hamamatsu R585 photomultiplier. The spectral response of this photomultiplier ranged from 160 nm to 650 nm. The detected wavelength was converted to energy (meV) using a index of refraction of 1.000289.

Chapter 3

Investigation of I_{10} luminescence

Several D^0X PL lines have been observed in ZnO, among which I_{10}, at 3353.4 meV, is one of the most poorly known. In this section we initially present two hypotheses on the origin of I_{10} with one including Li as one of the components of the defect associated with this emission and one without. Experimental measurement of the donor binding energy of the defect is presented and was compared to the theoretically expected values for each model. Annealing measurement under high purity nitrogen showed the I_{10} could be eliminated at high temperature. In addition, the results of diffusion of Li into the sample are provided and the correlation of the Li concentration with the intensity of I_{10} is studied. Evidence of a very small shift in emission energy on substitution of ^{7}Li with ^{6}Li is presented.

3.1 I_{10} shallow donor bound exciton PL

Fig. 3.1 shows a typical spectrum of high purity ZnO sharing a clear I_{10} line at 3353.4 meV in addition to several other shallow D^0X lines and their TES lines. A study by J. Cullen et. al [26] in 2013 conclusively associated I_{10} with tin impurities. In their study, a chain radioactive reaction of ^{117}Ag/^{121}Ag decaying to ^{117}Cd/^{121}Cd and then ^{117}In/^{121}In and finally to ^{117}Sn/^{121}Sn shows a gradual increase in I_{10} with time as the intensity of the Sn increases in the sample due to β decay. Further studies by our group at SFU have provided more evidence on association of Sn with I_{10} [27]. Sn-doped bulk crystal samples grown by the chemical vapor transport method showed stronger I_{10} luminescence compared to those unintentionally doped with the same method. However strong variations in the intensity of the I_{10} lines were observed even within the same sample growth.

Involvement of Li in I_{10} emission was first suggested in 1976. A study of near band gap PL in ZnO [28] attributed the I_{10} and another line at 3354.1 meV respectively to Li and Na neutral acceptor bound excitons, assuming Li and Na to be shallow acceptors. Later in 2004, a more dependable study [7] showed that I_{10} is a D^0X, although they did not deny the correlation of Li and I_{10}. In fact, Fig. 11 of their published paper [7] shows a considerable

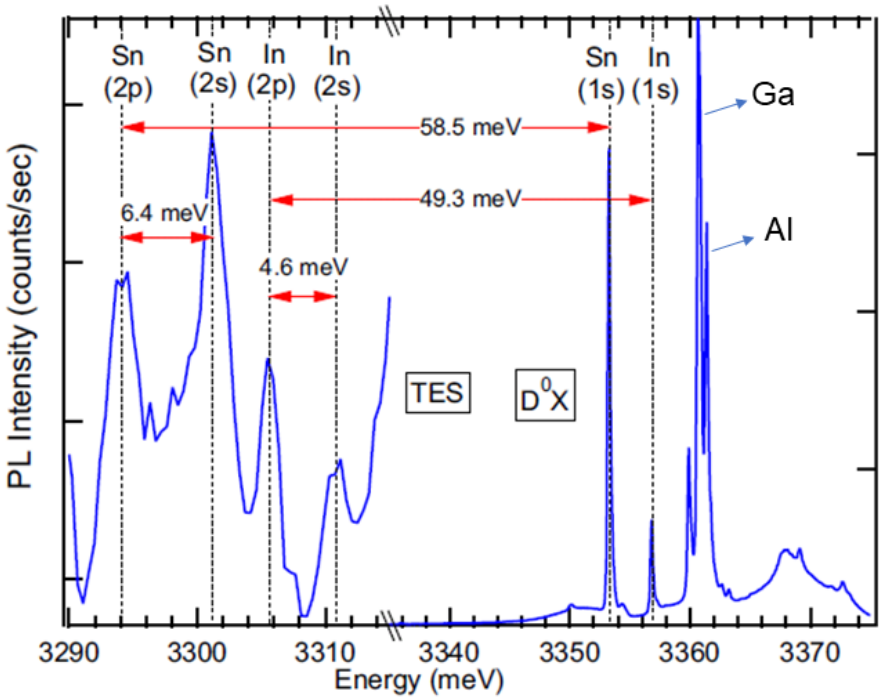

Figure 3.1: PL measurement of the TES region on a tin doped ZnO sample. This figure is from reference [27]

increase in I_{10} as a result of Li doping. Finally, after Sn was proved to be related to I_{10} in the same study [26] it was proposed that this emission is due to a defect complex consisted of Sn_{Zn} and a Li most probably a Li_{Zn}.

Sn_{Zn} is expected to be a double donor and Li_{Zn} is a deep single acceptor. A complex consisting of a Sn_{Zn}-Li_{Zn} would result in a possible single donor. Fig. 3.2 shows the positioning of atoms in a Li_{Zn}-Sn_{Zn} defect in a wurtzite ZnO lattice. A defect with only one atom Sn_{Zn} can also be imagined to be responsible for I_{10} which we will consider as a possibility, although during the course of this chapter it will be rejected.

3.2 Donor binding energy of I_{10}

In this section a comparison of the experimentally measured donor binding energy of I_{10} and theoretical values for single and double donors based on effective mass approximation (EMA) is presented.

As explained in section 1.1.3, the central cell potential of the donors results in a greater

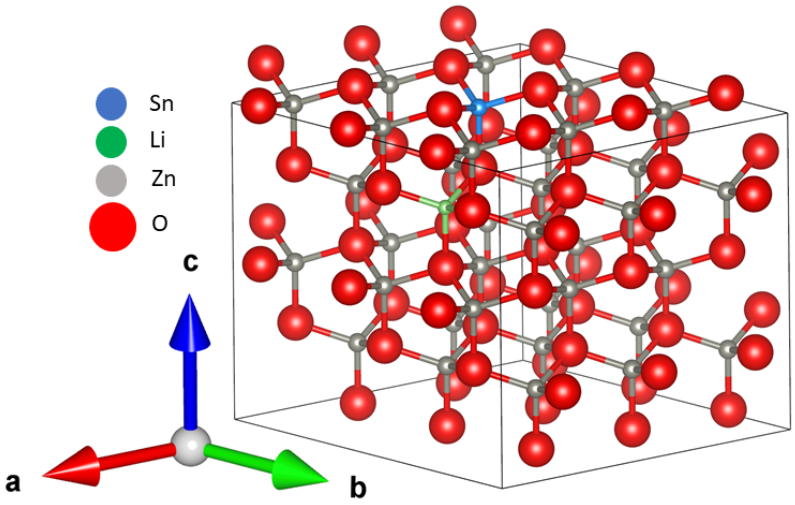

Figure 3.2: ZnO wurtzite structure containing a Li_{Zn}-Sn_{Zn} pair at the nearest neighboring Zn sites. The Li and Sn atom are bound to a common oxygen atom. Figure by Manu Hegde

donor binding energy than the EMA values. This difference appears in TES lines attributed to the I-lines. Fig 3.1, from a previous study in our group [27], shows the position of the 1s, 2s and 2p lines for I_9 and I_{10}. As a deeper donor, I_{10} shows a greater 1s-2p separation of 58.5 meV compared to 49.3 meV for I_9. Using Eq (1.7) we can find the donor binding energy of the D^0X lines from their 1s-2p separation. The EMA value for the single donor is explained in section 1.1.3 where the defect is treated as a hydrogen-like structure. For the case of a double donor we use a model based on a theoretical study by R. Marquez and C. Rincon [29]. This model is based on a helium-like model. The EMA equation for this situation would be

$$\begin{aligned}&\left[-\hbar^2/2m^*\left(\nabla_1^2+\nabla_2^2\right)-Ze^2/\varepsilon_0 r_1-Ze^2/\varepsilon_0 r_2\right.\\&\left.+\left(e^2/\varepsilon_0\right)\left(1/\left|r_1-r_2\right|\right)\right]F\left(r_1,r_2\right)=EF\left(r_1,r_2\right),\end{aligned}\tag{3.1}$$

where $F(r_1, r_2)$ is an envelope function for donors and indexes 1 and 2 refer to the electrons in the structure. Also $E = E_1 + E_2$, where E_1 and E_2 are binding energies of the first and second electron. A variational treatment yields

$$E_1 = 1.7e^4 m^*/2h^2\varepsilon_0^2 = 1.7E_D \tag{3.2}$$

$$E_2 = 4e^4 m^*/2h^2\varepsilon_0^2 = 4E_D,$$

where E_D is the EMA electron binding energy for the case of a single donor as in section 1.1.3. Table 3.1 shows the experimental values for several I-lines, including I_{10}, as well as the EMA based on theoretical values for single and double donors in ZnO. The values $\epsilon = 8.75$ and $m_e^* = 0.28m_0$ have been used for the dielectric constant and the electron effective

mass.

Table 3.1: Donor binding energy of the defects in ZnO associated with I-lines.

Element	I-line	Binding energy (meV)
Effective mass single donor	NA	50.15[7]
Al	I_6	51.6
Ga	I_8	54.6
In	I_9	63.2
Sn complex	I_{10}	72.6
Effective mass double donor (first electron)	NA	85.26

The experimental binding energy of I_{10} is 72.6 meV. This is significantly lower than the value of 85.3 meV predicted for an EMA double donor (Table 3.1). This evidence suggests that I_{10} is a single donor based defect, supporting the Li_{Zn}-Sn_{Zn} model.

3.3 Model for removal of Li from I_{10}

An important test of Li_{Zn}-Sn_{Zn} complex model is the effect of thermal annealing on the stability of the complex. In this section, we present two models based on two studies, one by T.N.Sky et al. on Li_{Zn}-Ga_{Zn} defects in ZnO [30] and the other by A. Carvalho et al. on Li in ZnO [31]. The ejection of the Li from its substitutional site to an interstitial site can happen through a dissociation of the Sn_{Zn} and Li_{Zn}, or alternatively a kick-out mechanism where an interstitial Zn kicks the Li_{Zn} out and replaces it. The activation energy for these processes have been calculated using DFT calculations and compared to the activation energy derived from experimental data. For the dissociation mechanism we have

$$(\mathrm{Sn_{Zn}Li_{Zn}})^{+} \rightarrow \mathrm{Li}_i^{+} + \mathrm{Sn_{Zn}V_{Zn}}, \tag{3.3}$$

and for the kick-out mechanism we have

$$(\mathrm{Sn_{Zn}Li_{Zn}})^{+} + \mathrm{Zn}_i^{2+} \rightarrow \mathrm{Li}_i^{+} + \mathrm{Sn}_{\mathrm{Zn}}^{2+}. \tag{3.4}$$

3.3.1 Dissociation mechanism

The process of the diffusion of Li through the dissociation mechanism and its reaction with Zn-vacancies in interstitial form the equation

$$\frac{\partial C}{\partial t} = KC_{Sn_{\mathrm{Zn}}V_{\mathrm{Zn}}}C_{\mathrm{Li_i}} - \nu C \text{ [30]}, \tag{3.5}$$

where C is the concentration of Li_{Zn}-Sn_{Zn} and $\mathrm{C}_{\mathrm{Sn_{Zn}-V_{Zn}}}$ and $C_{\mathrm{Li_i}}$ are the concentration of tin-vacancy pairs and interstitial Li respectively. $K = 4\pi R_c D_{\mathrm{Li}}$ is the formation rate of Li_{Zn} as a result of the reaction of Li_i with V_{Zn}, where R_c is the effective reaction radius and D_{Li} is the diffusion constant of ${\mathrm{Li}_i}^{+1}$. $\nu = \nu_0 e^{-E_d/k_B T}$ is the dissociation rate, where E_d is the dissociation energy barrier.

In the case of the Li_{Zn}-Ga_{Zn} impurity in Sky's study, after dissociation of Li, the remaining $(\mathrm{V}_{Zn}\text{-}\mathrm{Ga}_{Zn})^{-1}$ attracts the ${\mathrm{Li}_i}^{+1}$ ions in the sample. This results in a high effective reaction diameter R_c=1 nm [30]. R_c for our case with neutral V_{Zn}-Sn_{Zn} should be tremendously smaller than 1 nm, since there is no Coulombic attraction between the remaining defect and the ${\mathrm{Li}_i}^{+1}$ ions. Therefore, the recombination of ${\mathrm{Li}_i}^{+1}$ with V_{Zn}-Sn_{Zn} happens randomly which results in an R_c= 1.5 Å which is the radius of the substitutional site. That is because we assume as the Li atom passes the saddle point between the closest substitutional site and the closest interstitial site it will become trapped in the substitutional site. Thus, the term $KC_{V_{\mathrm{Zn}}}C_{\mathrm{Li_i}}$ on the right side of Eq. 3.5 is negligible, except when the Li atom is just removed from its substitutional site and it is very close to the neutral V_{Zn}-Sn_{Zn}.

We model the diffusion of Li out of the sample with a multi-step approach. If after the dissociation of the Li_{Zn}-Sn_{Zn}, the ${\mathrm{Li}_i}^{+1}$ travels far enough away from the V_{Zn}-Sn_{Zn} so that it is unlikely to go back to its initial position by a random walk, we consider it diffused out. The assumption that the Li_i will not be trapped in another V_{Zn} is pretty realistic in our case, especially because we treated the samples under N_2-rich conditions which is closer to Zn-rich condition, and hence should suppress V_{Zn} formation. In addition, as a result of the low penetration depth of the He-Cd laser in our PL setup we are basically only looking at the surface of the sample [see section 2.3.1] while the vapor pressure of Li is very high at the diffusion temperatures. This results in the instantaneous vaporization of the Li_i as soon as it is formed on the surface. For the vapor pressure we have:

$$\log_{10}(P) = A - (B/(T + C)), \tag{3.6}$$

where the pressure P is in bar and the temperature T is in Kelvin, and the parameters A, B and C for Li are 4.9883, 7918.98 and -9.52 respectively [32]. Fig 3.3 shows a diagram of the Li vapor pressure versus temperature based on Eq. 3.6, for temperatures between 600-900°C, where considerable changes in the intensity of I_{10} are seen. Eq. 3.6 yields values between 6.6×10^{-5} atm to 1.5×10^{-2} atm. These high vapor pressures should result in the efficient removal of Li from the surface after Li^+ ions turn to Li atoms after picking up an

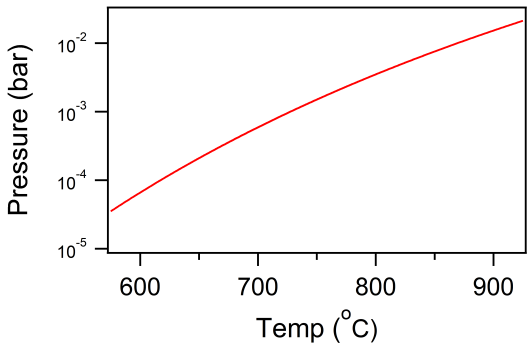

Figure 3.3: Vapor pressure of Li versus temperature.

electron from the conduction band.

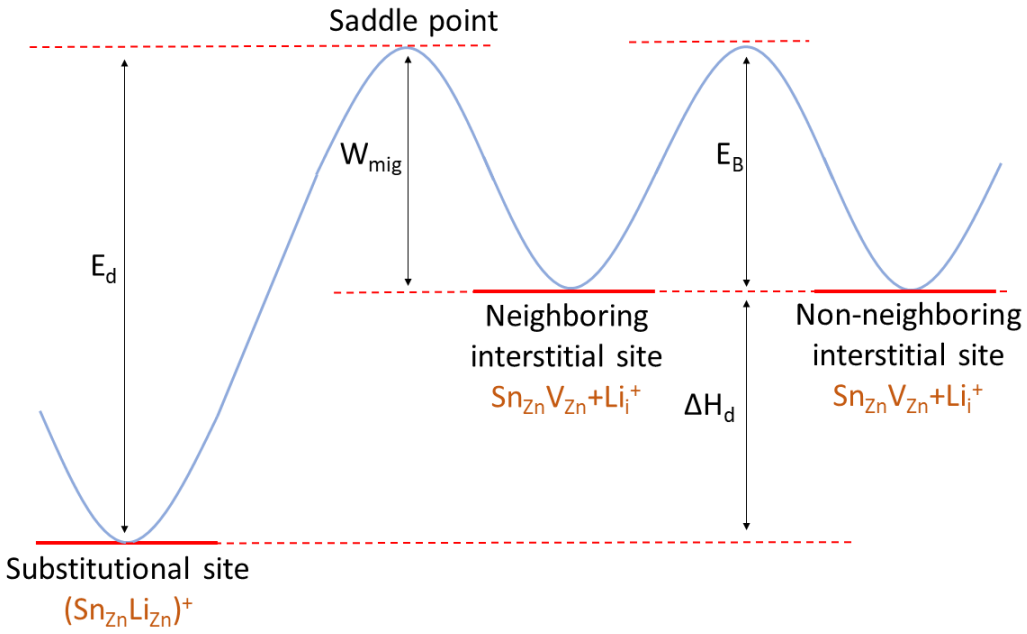

Figure 3.4: An energy diagram of the dissociation of Li from Li_{Zn}-Sn_{Zn} and its migration in the form of $\mathrm{Li}_i{}^{+1}$ away from the residual defect Sn_{Zn}-V_{Zn}.

In the first step of the dissociation model, the Li is removed from the Zn site and is found in one of the interstitial sites neighboring its initial position at a Zn site. This happens with a rate of $C\nu_0 e^{-\beta E_d}$, where $\beta = k_B T^{-1}$ and E_d is the total barrier energy for the dissociation process. Fig 3.4 shows a schematic of the situation. ΔH_d is the dissociation enthalpy and W_{mig} is the difference between the energy of the Li in the interstitial site and the saddle point on its path of migration to the substitutional site. Based on Fig. 3.4 for the E_d we

have:

$$E_d = \Delta H_d + W_{mig}(\mathrm{Li}_i) \tag{3.7}$$

ΔH_d can be derived from the formation energies of the two sides of Eq. 3.3:

$$\Delta H_\mathrm{d} = E_f\left(\mathrm{Sn_{Zn}V_{Zn}}\right) + E_f\left(\{\mathrm{Li}_i\}^+\right) - E_f\left(\{\mathrm{Sn}_{Zn}\mathrm{Li}_{Zn}\}^+\right) \tag{3.8}$$

Fig. 3.5 shows the DFT results calculated by Manu Hegde for the formation energies of the terms in Eq. 3.8. Based on the DFT results we obtained 3.2 eV and 3.5 eV for ΔH_d in O-rich and Zn-rich conditions respectively.

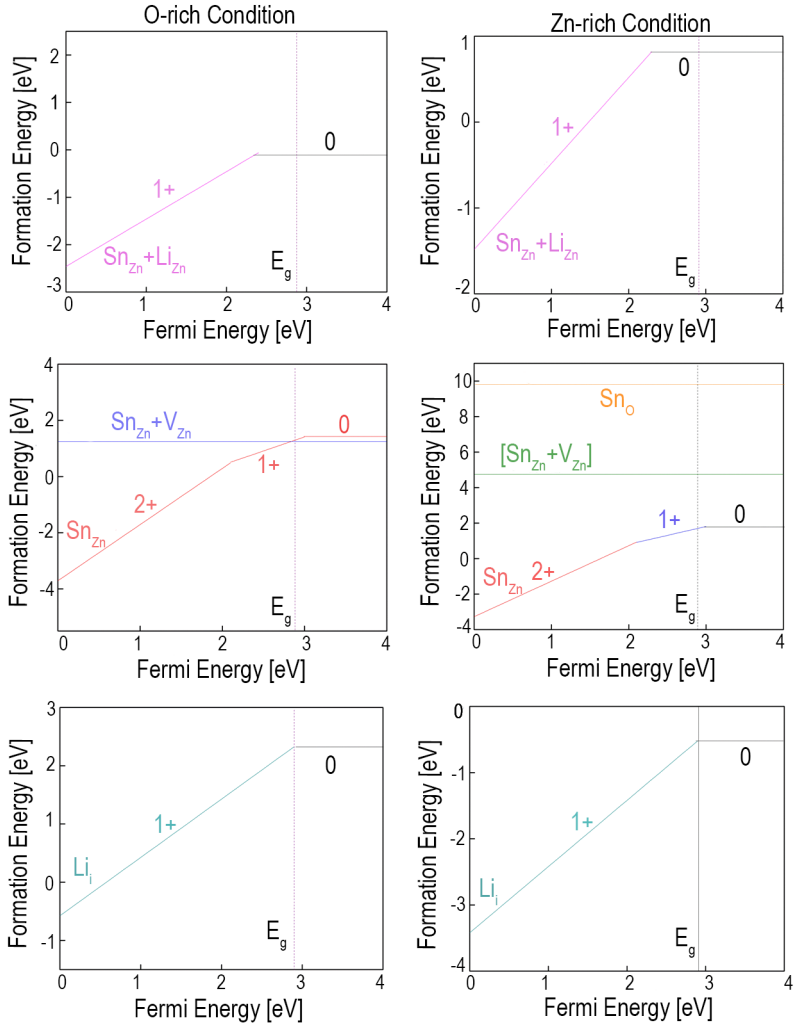

Figure 3.5: DFT results for the formation energies of certain defects in ZnO. All DFT simulations were done by Manu Hegde.

Dissociation of the Li from the $Sn_{Zn}Li_{Zn}$ is not enough to consider the Li atom diffused out of the sample, in that it is adjacent to the vacant Zn site. Hence, there is a high probability of the now interstitial Li^+ traveling back to its initial Li_{Zn} position.

There are three possibilities for the next movement of the Li^+ after it reaches a neighboring interstitial site. It can hop to one of the n other neighboring interstitial sites adjacent to its current site, or it can hop into one of the m interstitial sites further away from the Zn-vacancy. Also, it can hop into its previous substitutional site. Since the migration barrier E_B is very close to W_{mig} all of these cases happen with similar probability. The migration barrier energy E_B is the difference between the energy of the $Li_i{}^{+1}$ at its equilibrium position and the saddle point of its migration path [33]. Fig 3.4 shows a schematic of the E_B as well. Any migration after the dissociation of Li_{Zn}-Sn_{Zn} happens with an equal probability proportional to $e^{-\beta E_B}$. Thus, each migration happens with probability of $P = 1/(m+n+1)$. The total probability for a favorable migration away from the V_{Zn}-Sn_{Zn} is $mP = m/(m+n+1)$. The total probability for a migration to another neighboring interstitial site is $nP = n/(m+n+1)$, and finally traveling back to the Zn-vacancy just happens by the probability of P.

In order to consider the Li atom to be far enough from the Zn-vacancy we require it to only have one more migration to another interstitial site further away from the Zn-vacancy. This is enough because in this position the $Li_i{}^{+1}$ is almost 0.5 nm away from the V_{Zn}, which is still much bigger than $R_C << 1$ nm.

Let's say a dissociated $Li_i{}^{+1}$ migrates to another neighboring interstitial site i times before migrating to a non-neighboring interstitial site. The probability of this would be $(nP)^i mP$. Summing this probability for all possible i, $P_{total} = mP\sum_{i=0}^{\infty}(nP)^i$, yields the total probability of $Li_i{}^{+1}$ migrating far away from the V_{Zn}-Sn_{Zn}. Therefore, for the diffusion rate of Li we have:

$$\begin{aligned}\frac{dC}{dt} &= -C\nu_0 e^{-\beta E_d} mP \sum_{i=0}^{\infty}(nP)^i \\ &= -C\nu_0 e^{-\beta E_d} mP\left(\frac{1}{1-np}\right) \\ &= -C\nu_0 e^{-\beta E_d}\left(\frac{m}{m+1}\right) \\ &= -C\nu_0' e^{-E_d/k_B T}\end{aligned} \tag{3.9}$$

The independence of this result from n is not unexpected in that the n migration possibilities to other neighboring sites do not affect the configuration. As long as we are waiting for a final migration to a non-neighboring site or the Zn-vacancy those ineffective migrations can be neglected. Therefore, a total number of $m+1$ migrations are available and only one of

them results in return of the Li atom to the substitutional site and stops the diffusion of the Li atom out. Hence, the dissociated Li_i^{+1} with a rate of $(m)/(m+1)$ results in diffusion of the Li^+ out of the sample. Based on the Eq. 3.9 the final conclusion is that the dissociation energy is equal to E_d. Using Eq. 3.7 and value W_{mig}=0.8 [31], E_d is equal to 4 eV and 5.3 eV for the N-rich and O-rich condition respectively.

3.3.2 Kick-out mechanism

A schematic of the energy diagram for the kick-out process (Eq. 3.4) is shown in Fig. 3.6. The process starts with the formation of Zn interstitial with very large formation energy and

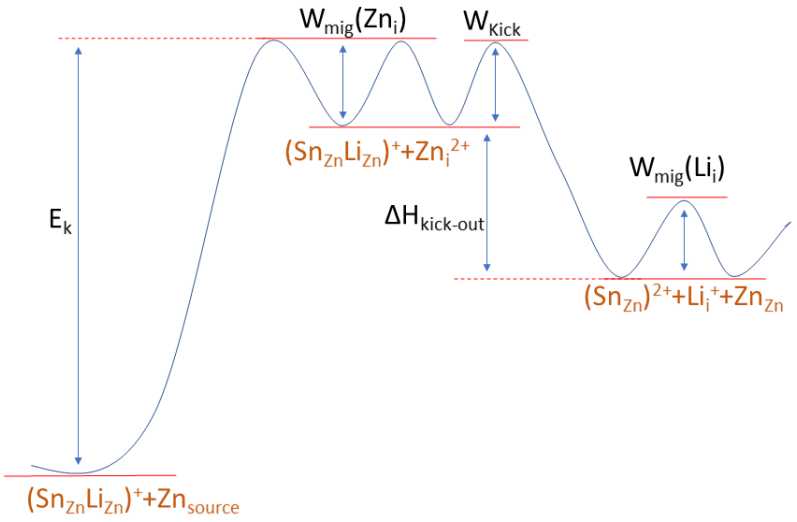

Figure 3.6: A schematic energy diagram for substitutional Li diffusion via kick-out by interstitial Zn [31].

then the substitution of it with Li_{Zn}. The enthalpy of the substitution when the interstitial Zn is in the interstitial site nearest to the Li_{Zn}-Sn_{Zn} is given by:

$$\Delta H_{\text{kick-out}} = E_f\left(\text{Sn}_{Zn}^{2+}\right) + E_f\left(\text{Li}_i^{+}\right) - \left[E_f\left(\text{Sn}_{\text{Zn}}\text{Li}_{\text{Zn}}^{+}\right) + E_f\left(\text{Zn}_i^{2+}\right)\right] \tag{3.10}$$

Eq. 3.10 yields -3.4 eV and -2.6 eV for the enthalpy of the kick-out reaction for O-rich and Zn-rich conditions respectively, based on DFT calculations by Manu Hegde. In both situations it is an exoenthalpic process, therefore the activation energy of this process is W_{Kick}= 0.8 eV [31] which is the difference between the energy of interstitial Zn and the saddle point on its migration path into the substitutional site. Therefore, W_{Kick} is expected to be very close to the $W_{mig}(\text{Zn}_i)$ [31].

For the formation energy of the Zn_i we have:

$$E_k = E_f\left(\text{Zn}_i^{+2}\right) + W_{\text{mig}}\ \left(\text{Zn}_i^{+2}\right) \tag{3.11}$$

Using the DFT data from Fig. 3.7 and W_{mig}= 0.8 eV [31], Eq. 3.11 yields 7.8 eV and 4.8 eV for E_k for both O-rich and Zn-rich conditions respectively. This shows a very endoenthalpic reaction.

Since E_k is much larger than W_{Kick}, the kick-out reaction is limited by the formation

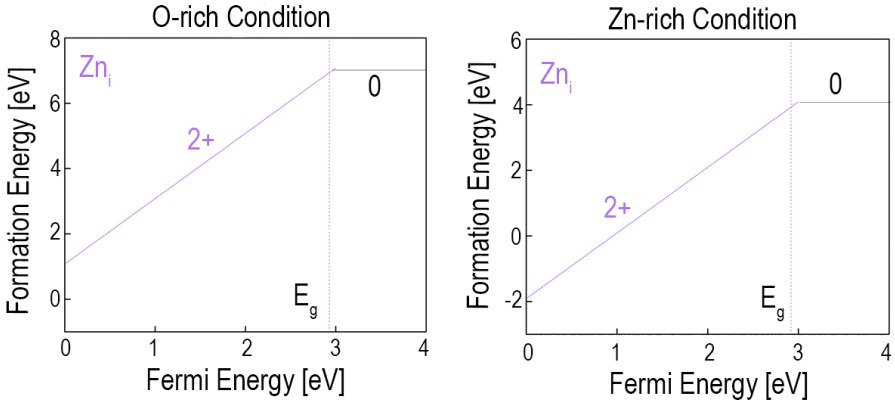

Figure 3.7: DFT results for the formation energy of Zn interstitial in ZnO.

of Zn interstitial. Therefore, the activation energy of the kick-out process is E_k i.e. 7.8 eV and 4.8 eV for O-rich and Zn-rich conditions respectively. Both of these values are greater than the activation energies calculated for the dissociation process. The dissociation process is clearly much more likely than the kick-out process for the removal of Li from the Sn_{Zn}-Li_{Zn} complex.

3.4 Experimental effect of annealing under N_2

We can test the preceding calculations by performing annealing experiments. As a result of annealing the samples at high temperatures, Li atoms are expected to dissociate from the I_{10} complex and occupy a highly mobile interstitial position, from where they can leave the crystal by diffusing to the surface. If Li is one of the components of the I_{10} defect it is expected that the I_{10} intensity will decrease following the annealing in N_2. An as-grown sample, A-1 with a high intensity I_{10} line was selected. The sample was annealed in a high purity MOCVD chamber at temperatures ranging from 450°C to 950°C. A 20 L/min(at room temperature) flow of N_2 kept the environment clean from impurities, especially oxygen molecules. Fig 3.8 shows the PL spectrum after each treatment. These results show that there is a significant broadening of the as-grown bulk crystals PL. This is due to non-uniform strain in the samples, which is reduced at higher annealing temperatures, resulting in a significant sharpening of the lines. Fig. 3.9 shows the full width at half maximum (FWHM) of I_9 and I_{10} in more detail for all the treatment temperatures as well as for the as-grown sample. It is worth noting that after 650°C the FWHM of the I_9 does not change

much, which shows that by 650°C almost all the lattice strain has been released. These linewidths are considerably broader than the value of about 10^{-6} eV estimated for homogeneous broadening on reported lifetime measurements [34]. Therefore, we assume that the lifetimes are limited by inhomogeneous mechanisms such as strain and donor interactions.

In order to study the I_{10} intensity we need to compensate for the effect of line broad-

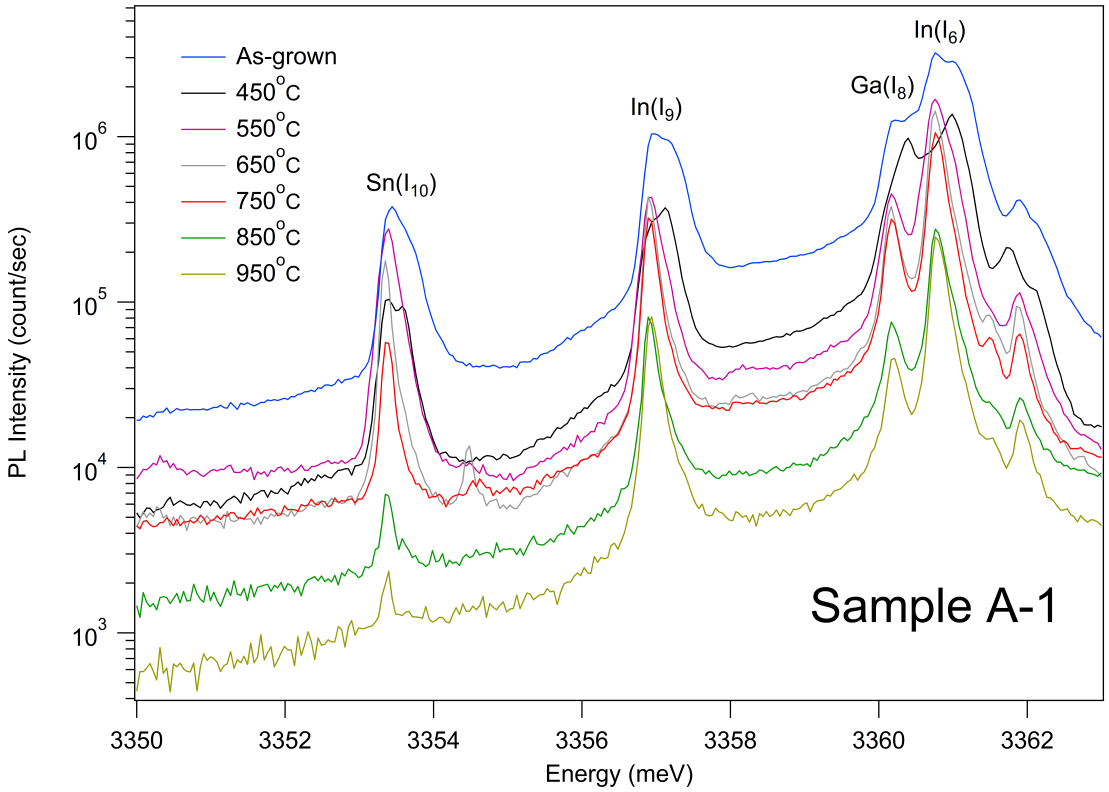

Figure 3.8: PL intensity variation of a sample with high I_{10} intensity annealed at temperatures from 450°C to 950°C under N_2-rich condition. Data acquisition by Manu Hegde

ening due to strain. Therefore, we used the integrated intensities of the lines as an indicator of their relative concentration. Lorentzian curves were fitted on the I-lines using the software Igor Pro 6.37, and used to calculate the integrated intensity. A Lorentzian curve gave a better fit than a Gaussian peak. An example of fitting can be found in Fig 3.11. The integrated intensity of I_{10} and I_9 after annealing in different temperatures is shown in Fig. 3.10(a). This figure shows a decrease in the intensity of I_{10}, but also in the intensity of I_9 as a result of annealing. We need to avoid the errors due to optimization of the PL system and possible overall changes in the intensity of the exciton region PL. Since I_9 is confirmed to be due to In, therefore independent from Li, we take its intensity as the reference and normalize the I_{10} intensity using I_9. The integrated intensity of I_{10} and I_9 after annealing in different temperatures is shown in Fig. 3.10.b. A decrease is still evident as a result of annealing.

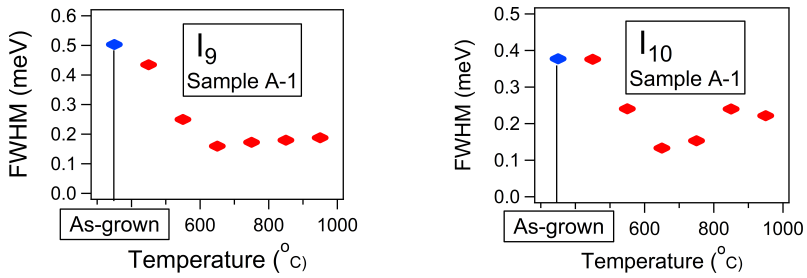

Figure 3.9: Variation of the full width at half maximum of I_9 and I_{10} line with annealing at temperatures from 450°C to 950°C. The blue data point is for the as-grown sample

This evidence supports the hypothesis of involvement of Li in I_{10}, since the removal of Li has resulted in a decrease in I_{10}.

Fig 3.12 shows a plot of I_{10}/I_9 intensity ratio versus $1/T$. A drop in the intensity ratio is evident with temperature increase. b is the slope and a is the y-intercept of the plot. This is evidence of the involvement of Li atoms in the I_{10} point defect.

Having this result, it is possible to evaluate the activation energy of the removal of Li from the V_{Zn}-Sn_{Zn} defect under N_2 gas using Eq. 3.9. For the reaction rate coefficient we have:

$$\begin{aligned} -\tfrac{dC}{dt}\tfrac{1}{C} &= \nu_0 e^{-E_d/k_B T} \\ \Rightarrow \quad -\tfrac{dC}{C} &= \nu_0 e^{-E_d/k_B T} dt \end{aligned} \quad , \tag{3.12}$$

which in a discrete form turns to

$$\begin{aligned} -\tfrac{\Delta C}{C} &= \nu_0 e^{-E_d/k_B T} \Delta t \\ \Rightarrow \ln(-\tfrac{\Delta C}{C}) &= \ln(\nu_0 \Delta t) - \tfrac{E_d}{k_B}\tfrac{1}{T} \end{aligned} \tag{3.13}$$

This equation shows a linear relation between the logarithm of $-\frac{\Delta C}{C}$ and the inverse of the temperature. Assuming that line intensities are proportional to the defect concentrations a similar linear equation can be written for the I_{10} integrated intensity:

$$\begin{aligned} \ln(-\tfrac{\Delta I_{10}}{I_{10}}) &= \ln(\nu_0 \Delta t) - \tfrac{E_d}{k_B}\tfrac{1}{T} \\ \Rightarrow \ln(-\tfrac{\Delta I_{10}/I_9}{I_{10}//I_9}) &= \ln(\nu_0 \Delta t) - \tfrac{E_d}{k_B}\tfrac{1}{T} \end{aligned} \tag{3.14}$$

where the second line is the same equation with I_{10} normalized by I_9. I_{10} and I_9 are the integrated intensity of the I_{10} and I_9 respectively.

Fig. 3.12 shows a linear fit to $\ln(-\frac{\Delta(I_{10}/I_9)}{I_{10}/I_9})$ versus inverse temperature. The slope of the plot gives $\frac{-E_d}{k_B}$ as in Eq. 3.14. Determination of the activation energy from the slope gives

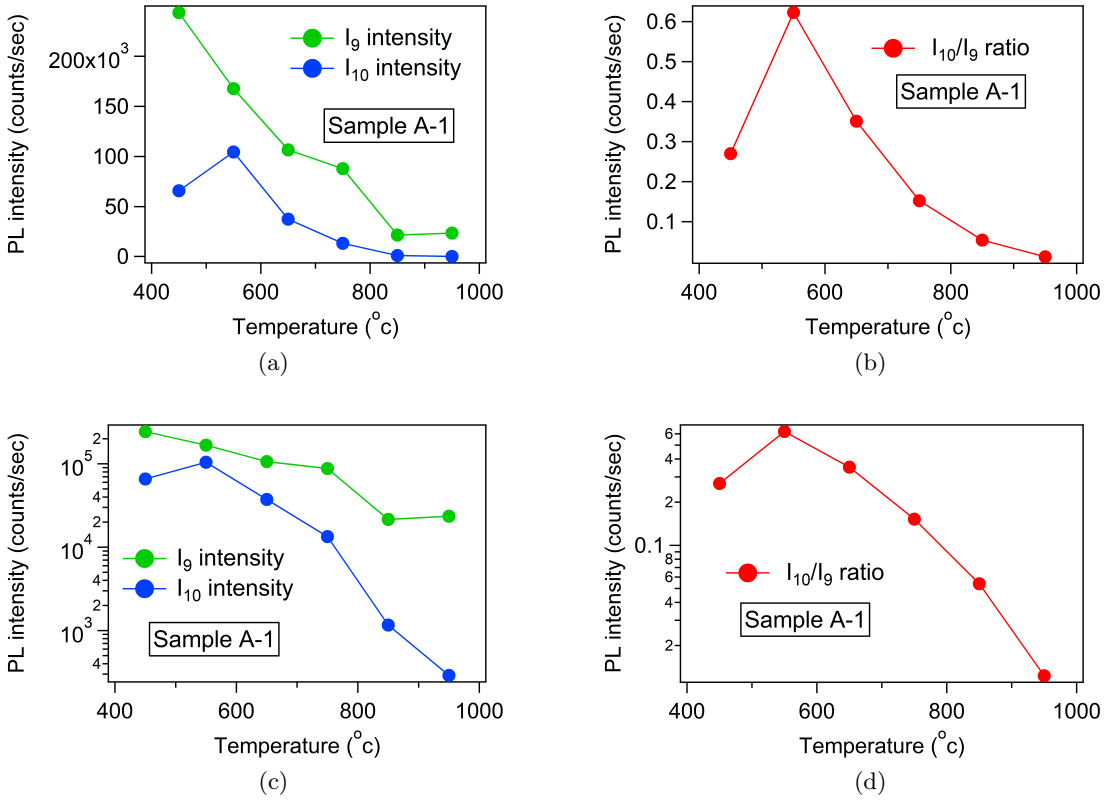

Figure 3.10: a) Variation of the integrated intensity of I_9 and I_{10} line with annealing at temperatures from 450°C to 950°C under N_2. b) Variation of the ratio of the integrated intensity of I_9 and I_{10} line with annealing at temperatures from 450°C to 950°C. c) Same as (a), but with logarithmic vertical axis. d) Same as (b), but with logarithmic vertical axis.

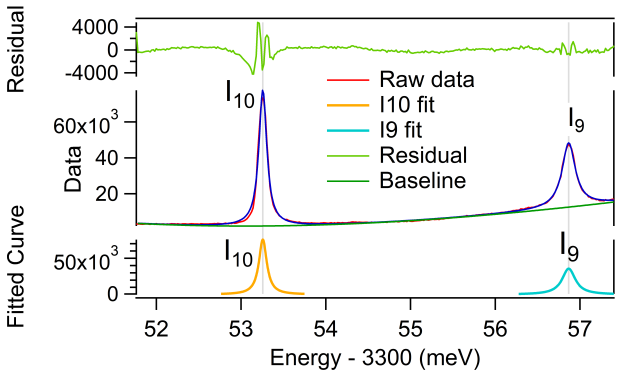

Figure 3.11: Lorentzian peaks fitted to I_9 and I_{10} to determine the position and intensity of the lines with more precision. A cubic curve was used for the baseline.

E_d= 0.4 eV ± 0.2. In addition using the y-intercept and Δt = 3600 secs (1 hour), for the attempt frequency we have $\nu_0 = 4.2\times10^{-2}$ s^{-1}. This value is much lower than the value observed by Sky et al. for dissociation of Ga-Li 5×10^{-13} s^{-1}. The physical significance of

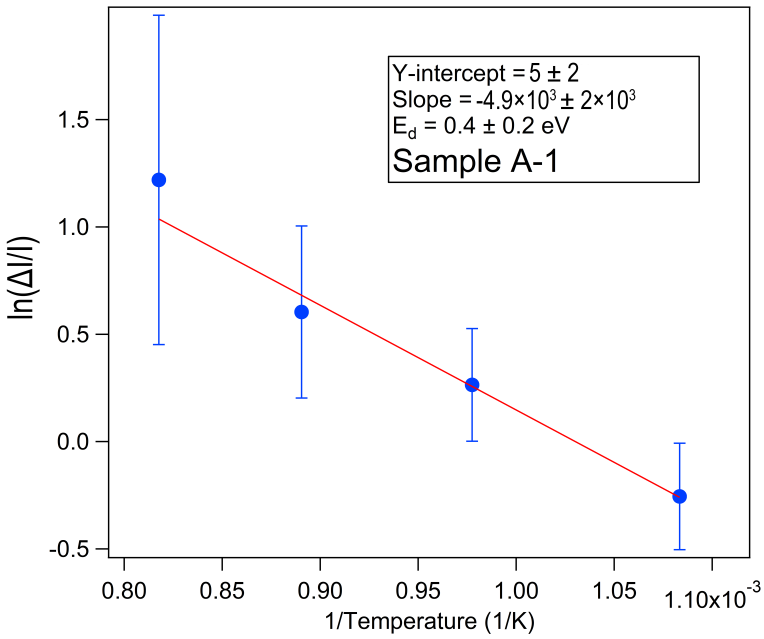

Figure 3.12: Normalized PL intensity ($I = I_{10}/I_9$) variation of a sample with high I_{10} intensity, annealed at temperatures from 450°C to 950°C versus 1/T.

this low attempt frequency is not clear. This value of E_d shows a large discrepancy with the DFT results of 4.8 eV and 3.5 eV respectively for the kick-out mechanism and dissociation mechanism. Therefore, it suggests that our picture of the structure of the I_{10} defect is not correct and the actual defect might be more complicated and have more components in addition to Sn and Li.

3.5 Effect of Annealing under O_2 On ZnO

In this section the results of annealing Sn-doped ZnO samples under O_2-rich conditions is presented. Similar to section 3.4, the samples were coated as explained in section 2.2.1 and annealed in a high purity MOCVD chamber at temperatures ranging from 400°C to 900°C increasing by 50°C steps. A flow of O_2 gas was used to keep the environment clean from other impurities. Fig 3.13 shows the PL result of the sample after each treatment.

Fig 3.14 shows the variation of the I_{10} and I_9 as well as their ratio as they change by successive treatments. Fig 3.14.a shows a drop in both lines as the temperature is increased. It is worth noting that similar to section 3.4, as a result of annealing a strain relief has caused the peaks sharpen up after the first treatment at 400°C. Therefore the integrated intensity was used to measure the strength of each line (see section 3.4 for the method).

Fig 3.14.b shows a much lower decrease in I_{10} compared to Fig. 3.10 for N_2-rich condition, which is in agreement with previous research that shows a much larger diffusion coefficient for Li in Zn under O_2-rich condition compared to N_2-rich [35]. This is also in agreement with our DFT calculation of the activation energy of the removal of Li from I_{10}. For both processes, the kick-out process and the dissociation process a larger activation energy was calculated for O_2-rich condition which results in lower removal of Li from the sample. An almost steady I_{10}/I_9 ratio was observed until 800°C. After 800°C there is a sudden drop in the I_{10} as well as the I_{10}/I_9 ratio. Fig 3.13 shows a drop of I_{10} at 850°C and 950°C to close to zero intensity. At 850°C the I_{10} intensity was not detectable and we were not able to fit a Lorentzian curve on I_{10}. Therefore the value 1 was used as its integrated intensity. This sudden drop at 850°C is in agreement with a previous study of Li diffusion in Ga-doped ZnO under O_2-rich condition [30]. Their data shows very low Li_{Zn} diffusion at 800°C and below, while at 850°C and above they observed a considerable diffusion of Li_{Zn}.

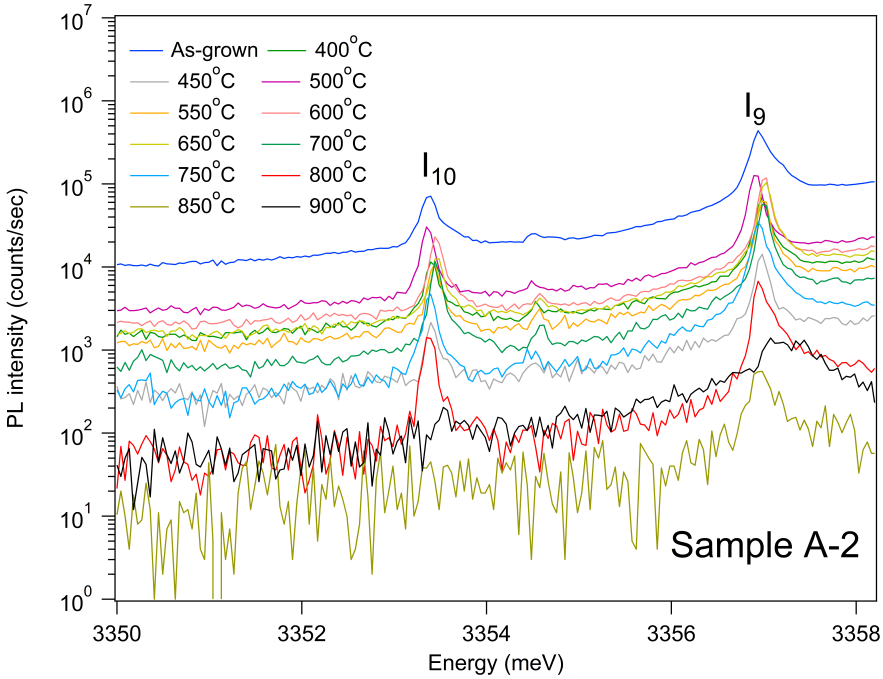

Figure 3.13: PL intensity variation of sample A-2 with high I_{10} intensity annealed at temperatures from 400°C to 900°C under O_2-rich condition.

3.6 Effect of Li diffusion on I_{10}

The diffusion of Li into Sn doped zinc oxide samples had a significant effect on the intensity of the I_{10} line. There were several other effects on the exciton region PL which are going to be elaborated upon in the next chapter. A significant increase in the intensity of the I_{10} line was observed in certain samples with low initial I_{10} intensity, after Li diffusion. Also,

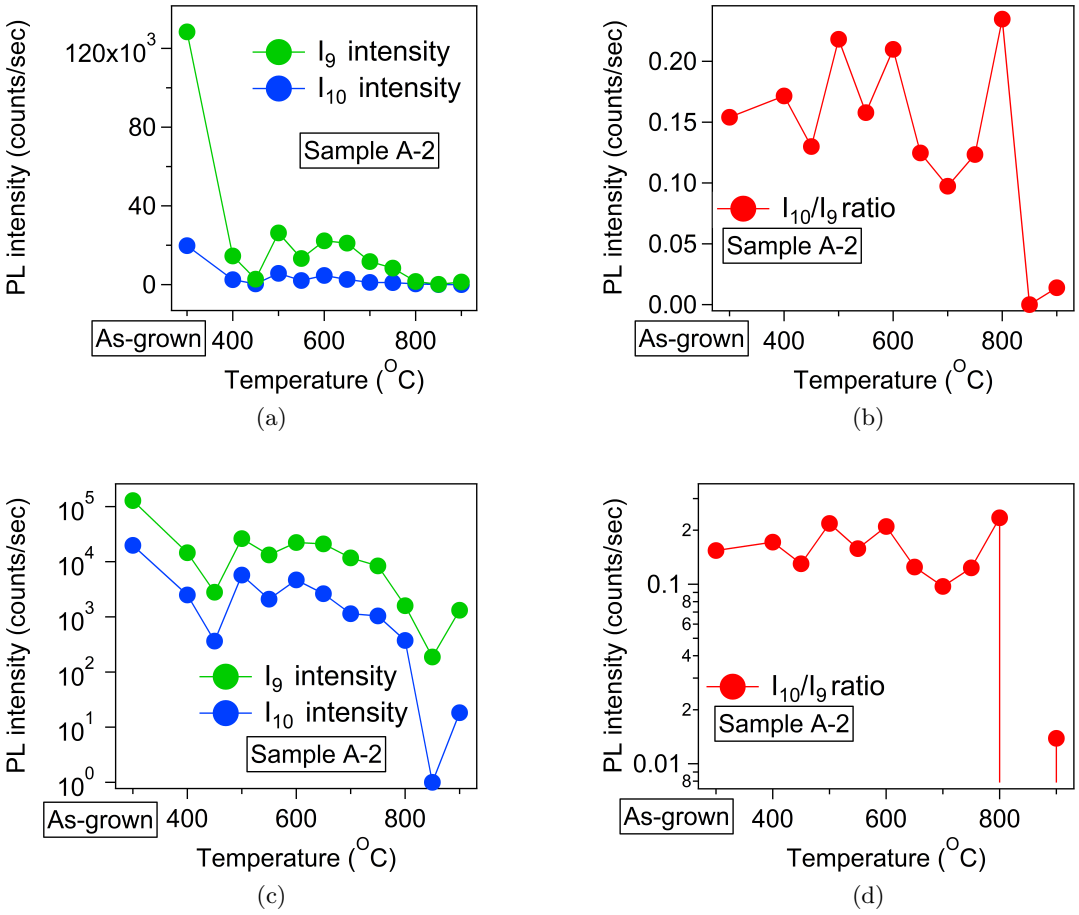

Figure 3.14: a) The effect of annealing on Sn-doped ZnO samples under O-rich conditions at temperatures from 400°C to 900°C on the I_{10} and I_9 integrated intensity. b) The effect of annealing Sn-doped ZnO samples at temperatures from 400°C to 900°C on the I_{10}/I_9 integrated intensity ratio in sample A-2. c) Same as (a), but with logarithmic vertical axis. d) Same as (b), but with logarithmic vertical axis. The data point at 850°C is zero. Due to very low intensity we were not able to fit any peak.

we will show examples of saturation of the I_{10} PL following Li diffusion which shows the involvement of a limiting element. This can be attributed to Sn, as previous research has proven the involvement of Sn in the I_{10} [26].

By the methods explained in sections 2.2, Li atoms were diffused into the bulk crystal sample used for annealing in section 3.4. The treatments was performed based on the method explained in section 2.2 at 450°C.The diffusion was done in an MOCVD chamber under a 20 L/min (standard T and P) flow of N_2 gas for 1 hour.

Fig 3.15 shows the PL spectrum of sample A-1 from section 3.4 after various heat treatments

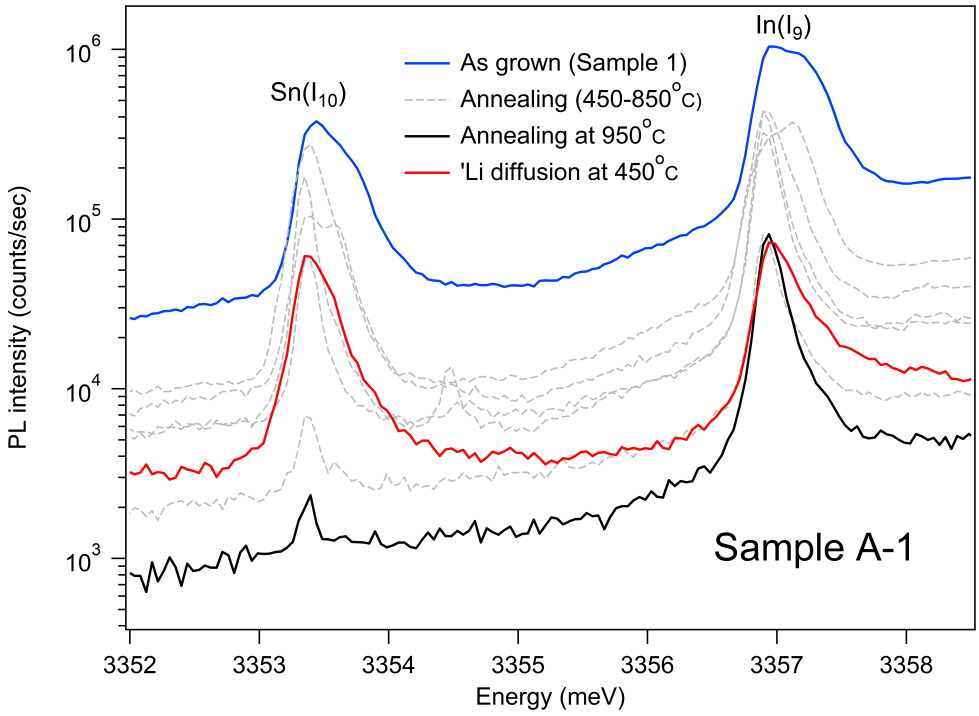

Figure 3.15: Effect of annealing and Li diffusion on a PL of a Sn-doped bulk crystal sample.

and diffusion. The as-grown sample (blue plot) was annealed under N_2 at temperatures from 450°C to 850°C (gray dashed plots) and finally at 950°C. The last annealing almost completely removed the I_{10} line. Subsequent Li diffusion at 450°C (red plot) resulted in a 147 times increase in the I_{10} peak intensity while little change in I_9 was observed. To further refine the measurement, we used the integrated intensity [see section 3.4]. As a result, an increase of 109 times in the I_{10}/I_9 ratio was measured from Fig 3.15, which is still a considerable increase. Comparing with the I_{10}/I_9 ratio of the sample after the first annealing at 450°C, an increase of 1.3 times was observed. We could not compare with the as-grown sample because of the broadening caused by strain.

Following the 450°C Li diffusion, a 550°C diffusion was done on sample A-1 to find out if more Li content will further increase the intensity of I_{10}. Fig 3.16.a shows an overall drop in the PL intensity and a negligible decrease of the I_{10}/I_9 ratio from 0.86 to 0.72. This suggests that the sample was saturated after the first diffusion. This saturation was expected since we know that Sn is a component of the defect which limits the intensity, independent from the Li concentration.

We repeated the Li diffusion on sample A-3 this time without removing the I_{10} by annealing. Sample A-3 is from the same growth as sample A-1. Fig 3.16.b shows the PL spectrum of this experiment. The as-grown sample shows very similar PL to A-1 as expected. The Li

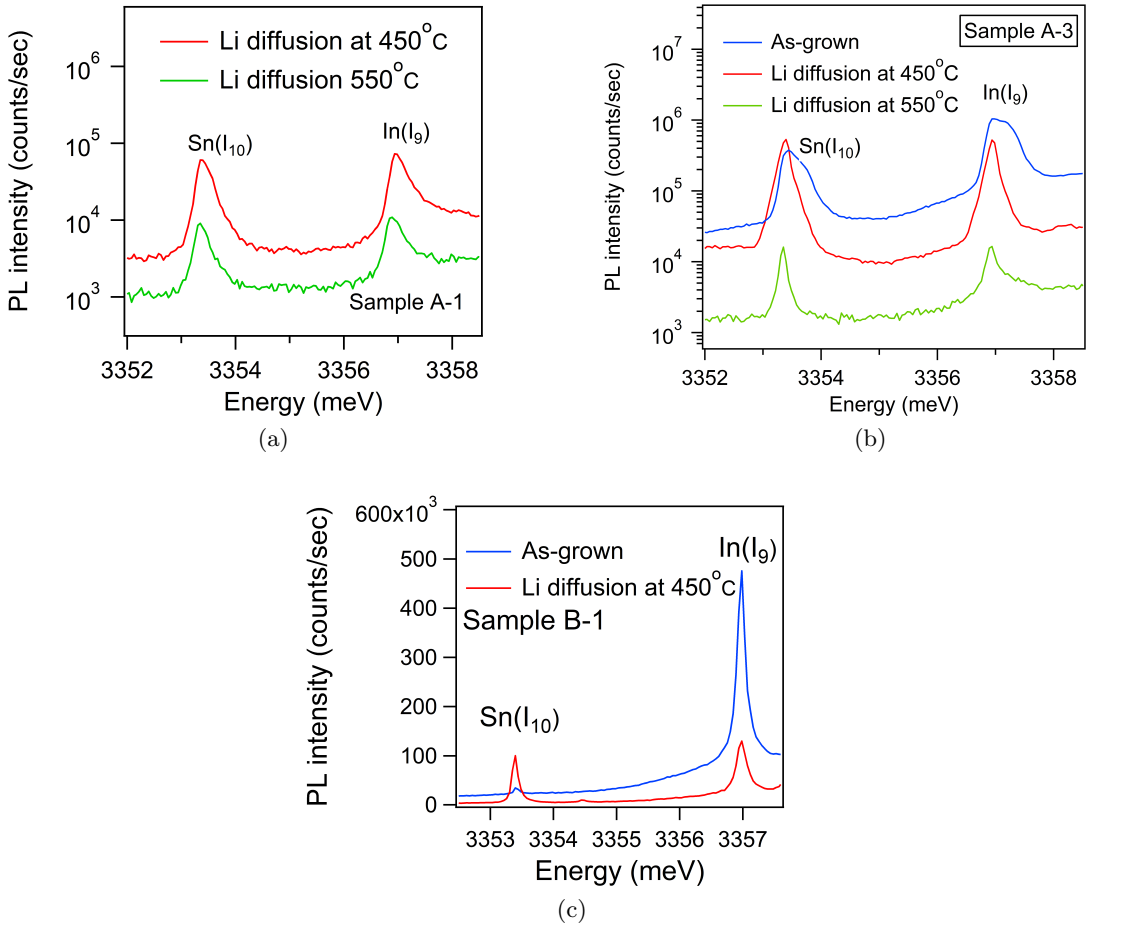

Figure 3.16: a)Effect of Li diffusion at 550°C on I_{10} in sample 1. This sample was previously Li diffused at 450°C as in Fig 3.15. b) The effect of Li diffusion on I_{10} line of sample A-3,a sample from the same growth as sample A-1, at 450°C. c) The effect of Li diffusion on I_{10} line of sample B-1, an unsaturated sample from a growth different from that of sample A-1 and A-3, at 450°C.

diffusion at 450°C shows a small increase in the I_{10}/I_9 ratio. This shows the sample was close to Li saturation as grown. A second diffusion at 550°C shows a negligible drop in the I_{10}/I_9 ratio similar to A-1.

In order to further prove the consistency of the results we performed a Li diffusion on another Sn-doped sample from a different growth with a low as-grown I_{10} intensity which we labeled B-1. Fig 3.16(c) shows the PL measurement of sample B-1 before and after the diffusion. The as-grown sample shows a small I_{10}/I_9 ratio compared to A-1 and A-3. Li diffusion at 450°C increases the I_{10} intensity and brings up the I_{10}/I_9 ratio to 0.52 which is comparable to the I_{10}/I_9 ratio for sample A-1 and A-3 in the saturated state. This is consistent with both samples having a similar Sn concentration. A 23.5 times increase in

I_{10}/I_9 ratio was measured for this sample using fitted Lorentzian peaks.

In order to confirm the role of Sn in the I_{10} defect a similar Li diffusion process was performed on high purity tin-free ZnO nanowire samples grown by MOCVD at SFU. These samples were grown without intentional doping and contain residual amounts of Ga and In donors (I_8 and I_9). The PL spectrum of the original sample as well as after Li diffusion, Fig 3.17, showed no sign of I_{10} luminescence. The vertical lines in the figures designate the expected position of the I_{10} line. A small overall decrease in the PL was observed which is in agreement with the previous data.

In conclusion, the experimental evidence strongly supports the hypothesis that a com-

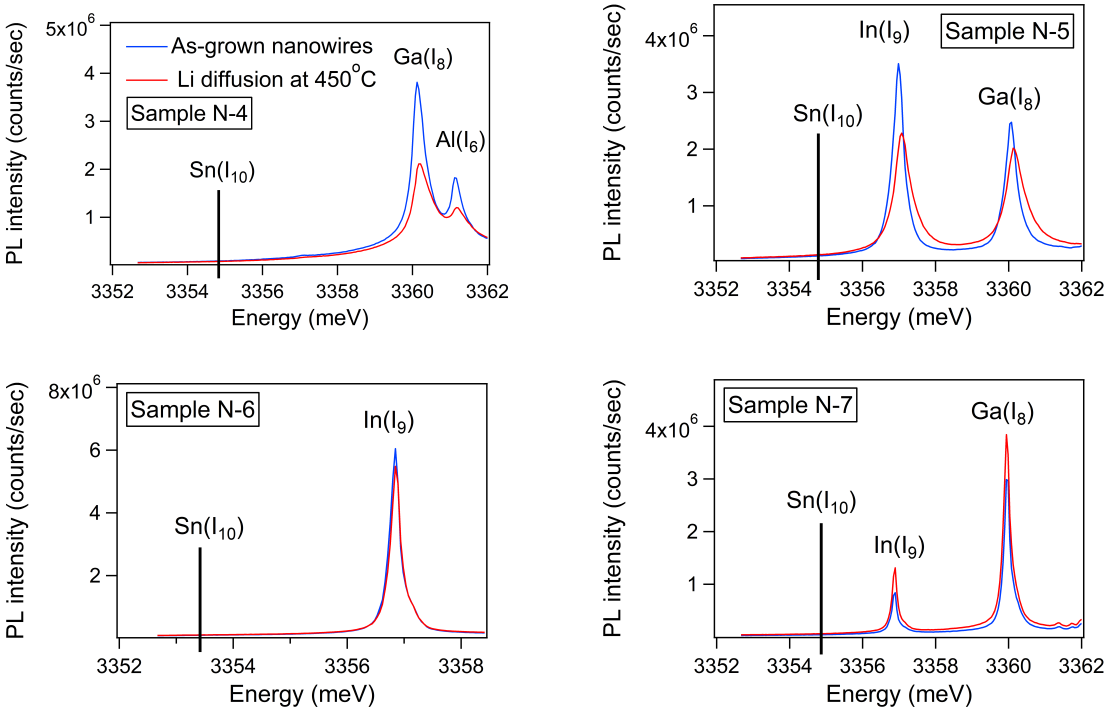

Figure 3.17: Effect of lithium diffusion at 450°C for 1 hour on four different Sn-free MOCVD grown ZnO nanowire samples with different background donor impurities.

plex of Li and Sn is responsible for the I_{10} luminescence rather than a simple Sn_{Zn} defect. Annealing of samples with I_{10} at high temperature in the presence of nitrogen gas results in the removal of the line, and an excess of Li doping restores it to a limit determined by the Sn concentration.

3.7 Effect of Li Isotope on the Energy of I_{10}

In this section, we further try to confirm the involvement of Li in the I_{10} luminescence. There is experimental and theoretical evidence, in many materials including ZnO, showing that the donor/acceptor bound exciton PL energy positions slightly shift by the isotope substitution of the impurity [21] [22] [36].

In the next section, we apply the model presented in section 1.3.1 that estimates the magnitude and the sign of the isotope shift. This model is based on the softening of the atomic bonds as a result of the presence of an electron or a hole carrier in the space between an impurity and its neighboring atoms [21]. This effect, coupled with the effect of the impurity's mass on the zero point vibrational energy of the defect, results in a PL emission shift due to the isotope of the impurity. In the experimental results section, we diffused in (^{7}Li) and (^{6}Li) to increase the I_{10} intensity in multiple samples and looked for an isotope shift in the I_{10} line.

3.7.1 Theoretical estimate of isotope shift for Li in ZnO

In section 1.3.1 we discussed a model for estimation of the isotope shift in the electronic transitions of defects. To find an estimate of the isotope shift for I_{10} we use Eq. (1.24). We first estimate P, the probability of an initial state electron being in the vicinity of the Li impurity where it causes softening of bonds with neighboring oxygen atoms. As an estimate of this we consider the extra electron of the initial state to add an extra charge equivalent to that of an isolated donor. We assume the hole of the exciton has negligible interaction with the defect core. P is defined as the probability that an initial state electron is localized over the spherical space enclosing the Li impurity on the Zn site and the four nearest O atoms. To estimate P we take the integral of the electron cloud density over this region.

$$P = \int_0^u \psi(r)^2 4\pi r^2 dr, \tag{3.15}$$

where u is the radius of the spherical region i.e. the Li-O bond and ψ is the wave function of the electron. Using 3D structure visualization software called VESTA [37] we found u/c is equal to 3/8 for an ideal wurtzite structure, where u is the length of the Li-O bond parallel to the c axis and c is the height of the unit cell in the c direction [see Fig. 3.18]. Using $c = 5.2$Å [9] gives $u = 1.95$Å. For the Bohr radius of the donor, we have $a_0 = 16.6$Å using simple effective mass approximation with $\epsilon = 8.75$ and $m_e^* = 0.28m_0$ for the dielectric constant and the electron effective mass respectively. Taking this integral from zero to u for the 1s orbital gives $P = 0.00179$ for an effective mass donor.

For the I_{10} defect, we have a 72.6 meV electron binding energy while EMA gives a value of 50.15 meV. The deeper the donor the more localized the wave function close to the core

would be, therefore, the deviation from EMT will be more considerable. This is treated using the concept of the "central cell potential". The addition of a central cell potential should result in an increased value to P since wave function will be more localized near the core.

To adjust the wave function to give the observed deeper binding energy, we perturb the core potential with a central cell potential. We use a spherical square quantum well at the impurity with a radius of $r_0 = 1.52$Å equal to the atomic radius of Li. Then we use non-degenerate perturbation theory to make an adjustment to the wave function. For the quantum well we have:

$$\delta V = \begin{cases} -V_0 & \text{for } 0 \leq r \leq 1.52\text{Å} \\ 0 & \text{otherwise} \end{cases} \tag{3.16}$$

We use the first order correction for the binding energy to find the depth of the quantum well that gives the observed spectroscopic donor binding energy. Since the difference in the binding energies emerges from the differences in the 1s orbitals we write the energy correction only for the 1s orbital.

$$E_1 = E_1^{(0)} + \langle 1s|V_0|1s\rangle + O\left(2\right), \tag{3.17}$$

where E_1 is the actual ground state energy and $E_1^{(0)}$ is the ground state energy without correction. Assuming $O\left(2\right)$ to be negligible we find V_0 by solving Eq. (3.17) for it. This results in a value of 11.2 eV for V_0.

Knowing the central cell potential correction we correct the wave function. We have:

$$|\psi_1\rangle = |1s\rangle + \sum_{k\neq 1s} |k\rangle \frac{\langle k|V|1s\rangle}{E_{1s} - E_k} + O(2) \tag{3.18}$$

Again we only correct the wave function to first order, neglecting the term $O\left(2\right)$. Since the p-orbitals have a node at the core they do not contribute to the sum. As the principal quantum number of the s orbital increases, the density of the electron cloud close to the core decreases and results in a smaller and smaller correction in Eq. (3.18). Calculating the correction only for the 2s orbital increases the original P to 0.00192. This shows an increase compared to the initial probability based on EMA which was 0.00179, as we expected. Adding the 3s term, we have $P = 0.00195$, which is a very incremental improvement. Therefore, since the rest of the terms are going to have a smaller contribution to the correction we neglect them.

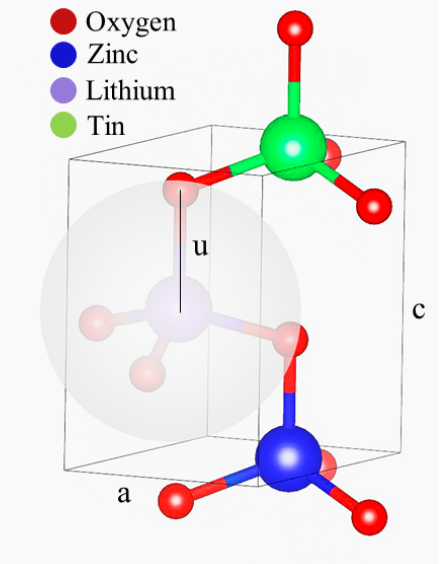

Figure 3.18: A schematic of wurtzite structure showing the area over which P has been integrated. The gray sphere shows the volume occupied by the impurity and its nearest neighbors

In the next step to evaluate Eq. 1.24, we find the term $\frac{dE_g}{dkT}$. The temperature dependence of the bandgap in semiconductors follows the empirical Varshni rule. In general, we have:

$$E_g = E_g^0 - \frac{\alpha T^2}{\beta + T}, \tag{3.19}$$

where α and β are constants specific to the material and E_g^0 is the band gap at zero temperature. For ZnO they are respectively equal to 0.00067 eV/K and 920 K [38]. Substituting α and β in the derivative of the Varshni equation and dividing it by k_B we have:

$$\left(\frac{dE_g}{dk_BT}\right)_{\text{HT}} = -\frac{(2\beta + T)}{k_B(\beta + T)^2}\alpha T = -3.3, \tag{3.20}$$

where HT stands for high temperature. HT is a temperature where $\langle n_i \rangle = kT/\hbar\omega_i$ is true [21]. The room temperature (292 K) is used as a high temperature. Substituting Eq. (3.20) and P in Eq. (1.24) gives $0.031\frac{\gamma_c}{\gamma}$ meV for the isotope shift. Considering that based on definition $0 < \frac{\gamma_c}{\gamma} < 1$, we expect a shift less than 0.031 meV. For the rest of the parameters we have substituted $M = M_{Li} = 6$ amu for the mass of ^{6}Li, $M_1 = M_O = 16$ amu for the mass of oxygen, $M_2 = M_{Zn} = 65.4$ amu for the mass of zinc, $M_0 = 25.7$ amu based on Eq. (1.25), $\Delta M = 1$ u for the mass difference between ^{6}Li and ^{7}Li and $\theta_D = 399.5$ K [39]. It is worth noting that the most abundant isotope of lithium is the ^{7}Li but since we take ΔM positive, ^{6}Li is taken as the original isotope and ^{7}Li as the altered isotope. The Sn component of I_{10} is in the neighboring site and we do not change its isotope systematically. This isotope shift is expected to affect the energy location of I_{10} such that the higher mass

isotope ^{7}Li results in a PL line at higher energies than for ^{6}Li. Since later we analyze our data based on the energy difference between I_{10} and I_9, it is worth noting that this would be interpreted as I_{10} appearing closer to I_9 for ^{7}Li compared to ^{6}Li i.e. smaller energy difference between I_9 and I_{10}.

3.7.2 Experimental results and discussion

In this section, we diffused Li into two series of samples with two different Li isotope contents, ^{7}Li and ^{6}Li. The lithium carbonate powder used as the sources of ^{7}Li was natural Li with 96% ^{7}Li and 4% ^{6}Li. The source used for ^{6}Li doping was isotopically enriched, containing 96% ^{6}Li and 4% ^{7}Li. For samples with ^{6}Li the lithium was diffused into the samples [see section 2.2] having a low initial I_{10} PL peak, and an increase of about 5 to 20 times in the I_{10} intensity was observed similar to Fig. 3.15. These samples are labeled S6-1,S6-2 and S6-3. Two of the samples with ^{7}Li were just samples with a high amount of residual Li in the as-grown condition that we consider to be natural lithium-doped, hence 96% ^{7}Li. They are labeled as SN-1 and SN-2. Sample SN-3 with initially low I_{10} PL peak was subjected to the same process as samples with ^{6}Li except they were treated with lithium carbonate with natural Li (96% ^{7}Li). Therefore all of the samples SN-1, SN-2 and SN-3 will have ^{7}Li with 96% purity. The I_{10} position was measured for all six samples using high resolution PL spectra.

To reduce the effect of the spectrometer drift by temperature fluctuations, we used the position of I_9 (In D^0X) as a reference, therefore, we reported the energy difference $E(I_9)$-$E(I_{10})$ to measure the isotope shift. The I_9 line is due to residual In point defects, therefore Li isotope doping would not have any effect on its energy.

For each sample we ran multiple PL scans, between 20 to 47 times, to reduce the random error in the peak position. The standard deviation of the mean of all of the $I_{10}-I_9$ energy separations was used as the error in table 3.2.

Lorentzian peaks were fitted to I_{10} and I_9 and a cubic curve was used to fit the background for each scan separately. The peak position separation of the fitted curves was used to measure the I_{10}-I_9 energy separations. The curve fitting was done using Igor Pro 6.37 (Wavemetrics, Lake Oswego, OR, USA). An example of the fitted curve is shown in Fig 3.11. Fig 3.19 shows the measured $I_{10}-I_9$ energy separation for all the samples separately after curve fitting the spectral peaks. The randomness in the position is considered to arise from two effects: first, temperature drifts in the lab environment are responsible for the overall shift observed over several hours. Second, there is clearly some randomness over shorter times that may be due to mechanical friction effects in the motor drive and associated gears.

The final results are presented in Fig 3.20 and Table 3.2. For the samples diffused with

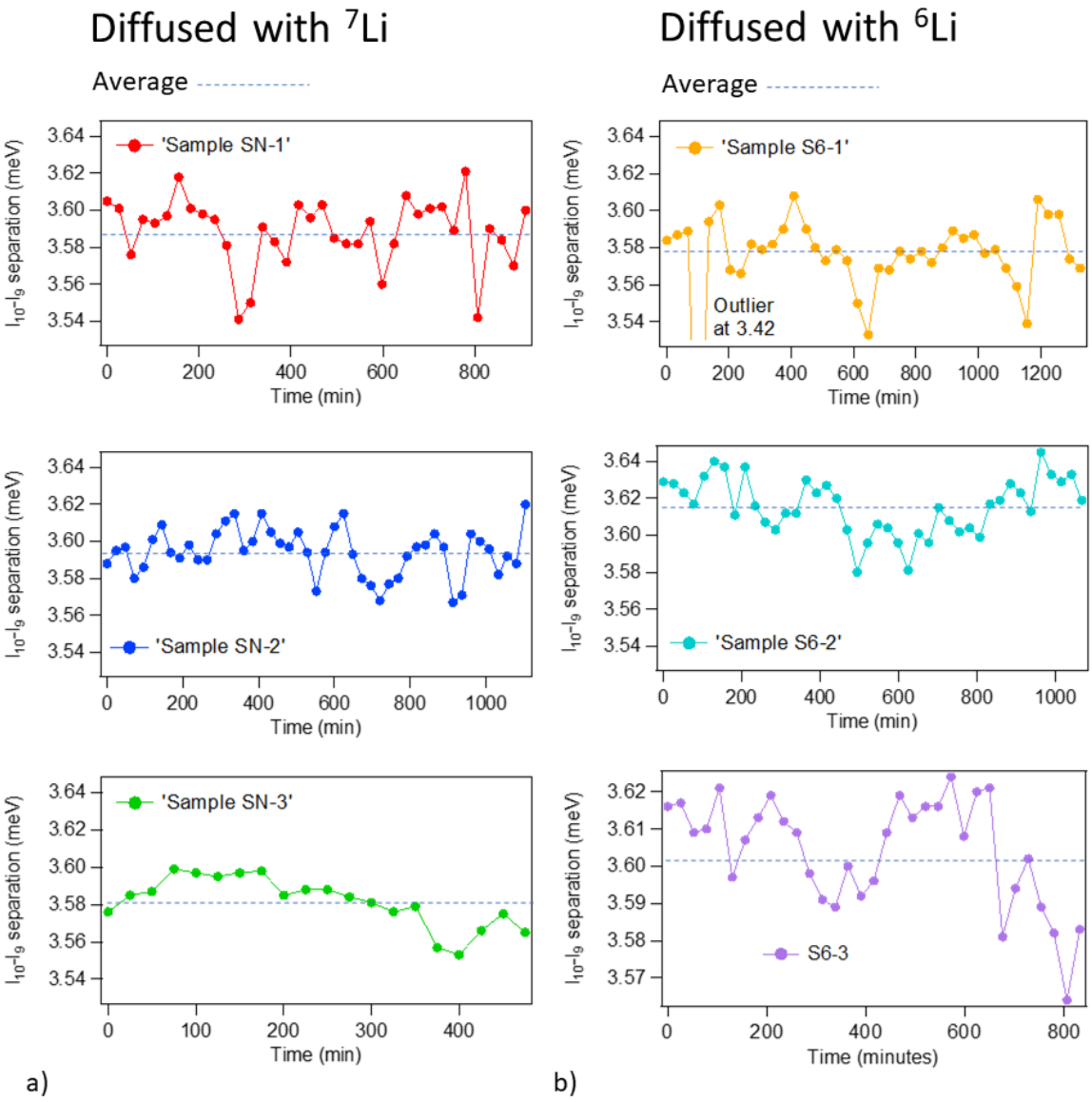

Figure 3.19: a) $E(I_9)$-$E(I_{10})$ for multiple scans on three samples with ^{7}Li. b) $E(I_9)$-$E(I_{10})$ for multiple scans on three samples with ^{6}Li. Note the very small energy range in the y-axis.

^{6}Li an average of 3.60±0.01 meV over all three samples has been measured. One of the points, sample S6-1, appears to be an outlier since it is far from agreement with the other two points. Excluding the possible outlier, the average would be 3.610±0.005 meV. For ^{7}Li all three data points are close to agreement with each other. The average $I_{10}-I_9$ energy separation is 3.588 ±0.004 meV. As expected there is a shift toward the higher energies for the ^{7}Li compared to ^{6}Li, which has resulted in a smaller $I_{10}-I_9$ energy separation for ^{7}Li. Upon replacement of ^{7}Li with ^{6}Li a shift of -0.01±0.01 meV and -0.022±0.008 meV has been

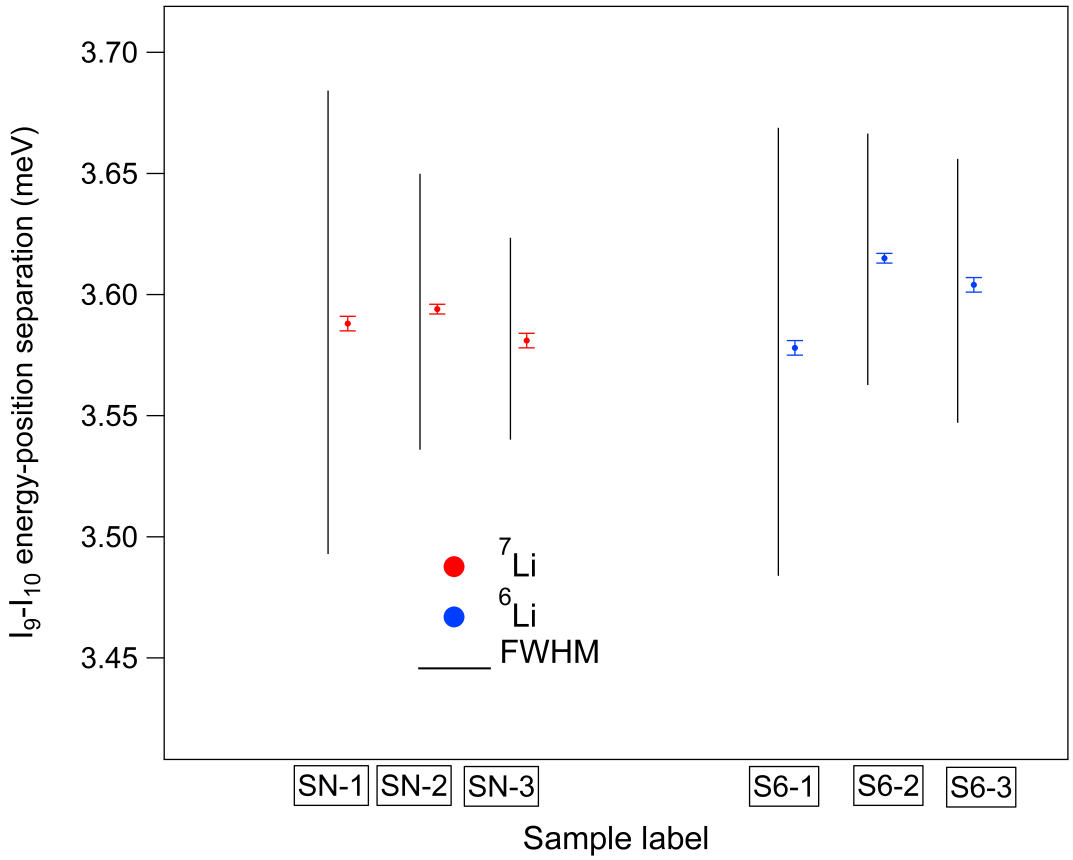

Figure 3.20: E(I_9)-E(I_{10}) for three samples with ^{6}Li and three samples with ^{7}Li. The length of the bars on the left of each data point shows the full width at half maximum of the I_{10} peak for that particular sample. The blue data point for ^{6}Li (sample 4) does not agree with the other blue data points. The data point for sample 4 can be identified as an outlier since it is at an energy difference even lower than the red data points for samples with ^{7}Li.

measured respectively including and excluding the outlier. Both of these results are consistent with the theoretical prediction in Section 3.7.1, which predicts a lower limit of -0.031 meV for the shift. Previous research on silicon has shown the same direction in isotope shift of bound exciton recombination energy with the decrease in the boron impurity isotope but one order of magnitude smaller in the amount of the shift[40]. Silicon donor bound excitons in GaP have shown similar isotope shift. A shift of 0.05±0.02 has been observed as a result of a substitution of ^{28}Si with ^{30}Si [41]. This shift is of the same order of magnitude as our result.

Table 3.2: Quantitative details for I_{10} position in samples SN-1, SN-2, SN-3, S6-1, S6-2 and S6-3.

Sample number	Li isotope	E(I_9)-E(I_{10}) (meV)	Separation Error(meV)	I_{10} FWHM (meV)	Number of data points
SN-1	7	3.588	0.003	0.192	36
SN-2	7	3.594	0.002	0.115	47
SN-3	7	3.581	0.003	0.084	20
S6-1	6	3.578	0.003	0.186	39
S6-2	6	3.615	0.002	0.105	42
S6-3	6	3.604	0.003	0.110	33

Chapter 4

Evidence of new Li-related lines

Li diffusion in certain tin-doped samples gave rise to new unidentified lines in the principal bound exciton region of the PL spectrum. More than ten of our experiments have shown the reproducibility of this result. The appearance of these lines in the BX region of the PL spectrum is convincing evidence that they are due to bound excitons. In addition to that, in section 4.2, we will provide stronger evidence of the excitonic origin of these lines based on Haynes' rule [see section 1.2]. Further discussion on the possible origin of the lines is provided. In addition, some details on the effect of the diffusion environment, Zn-rich (N_2 gas) or O-rich (O_2 gas), on the lines have been inferred.

4.1 L-lines

Fig. 4.1 shows the as-grown exciton region PL of a tin-doped sample as well as its spectrum after a Li diffusion. Lithium diffusion has given rise to several lines that we call L-lines and we labeled them from L_1 to L_8. The diffusion was done in a freshly cleaned chamber under a flow of N_2 gas at 450°C for 1 hour. The lithium source used for the coating was Li_2CO_3 enriched with ^{6}Li isotope, as in section 3.6. More experimental details on the conditions of the treatments can be found in section 2.2.

4.2 The excitonic nature of the L-lines and the Haynes' rule

To delve deeper into the nature of the L-lines, in this section we investigate whether the L-lines follow Haynes' rule for bound excitons. Based on this rule the donor/acceptor binding energy of the impurities and the localization energy of the donor/acceptor bound excitons have a linear relation [See section 1.2]. Haynes' rule is known to be obeyed for donors in ZnO very well [7][24][42].

Fig. 4.2 shows the plot of the TES region for one of the samples that has the largest

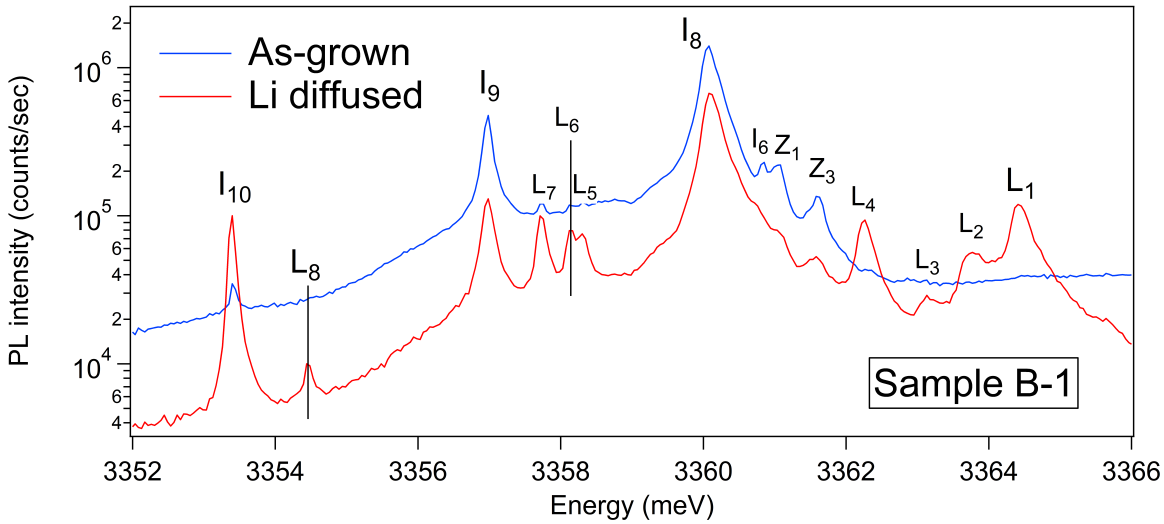

Figure 4.1: PL of tin doped ZnO sample before and after lithium diffusion.

number of L-lines. Several lines in the TES region have previously been correlated with I-lines [8] [7]. Among those TES lines, we observed the 2s and 2p lines for I_6, I_8 and I_9 in Fig. 4.2. Using the energy position of the 2s and 2p lines for the I-lines we were able to plot the 2s-1s as well as the 2p-1s transition for I-lines versus the localization energy of the D^0X. The plot shows a linear relation as expected from Haynes' rule Fig. 4.3. This plot was used for assigning the unknown TES lines appearing in our spectrum of the TES region to the L-lines. This matching was done based on how well the new TES lines would fit in the linear relations for I-lines if they were assigned to a certain L-line. The biggest deviation from the prediction of the linear fit was 1.3 meV for the 2p-1s separation of L_7. Table 4.1 shows quantitative details about L-lines as well as I-lines.

In Fig. 4.2, the I-lines and L-lines are labeled in black and green respectively and the lines that remained unidentified after assignment of L-lines are labeled in black with their energies in meV. Since the luminescence was very weak we had to average the count over a long time. The gray plot was done with 20 seconds exposure per wavelength point and the red plot, which is more smooth, with 160 seconds. As a result of the overnight exposure, the data might be subject to a small error of about 0.04 meV due to the spectrometer drift with ambient room temperature fluctuations. Fig 3.19 illustrates the magnitude and behavior of this error. It is worth mentioning that p orbitals are additionally split as a result of the anisotropy of the wurtzite structure. A separation of around 0.5 meV is expected between $2p_{xy}$ and $2p_z$, with the z direction being aligned with the c-axis of the wurtzite structure [7][43]. While some of the 2p lines, such as L_5(2p), L_6(2p), L_7(2p) and Al(2p), seem to show a structure compared to their corresponding 2s lines, no splitting has been clearly resolved. The inset of Fig. 4.2 shows the location of the L-lines in the exciton region.

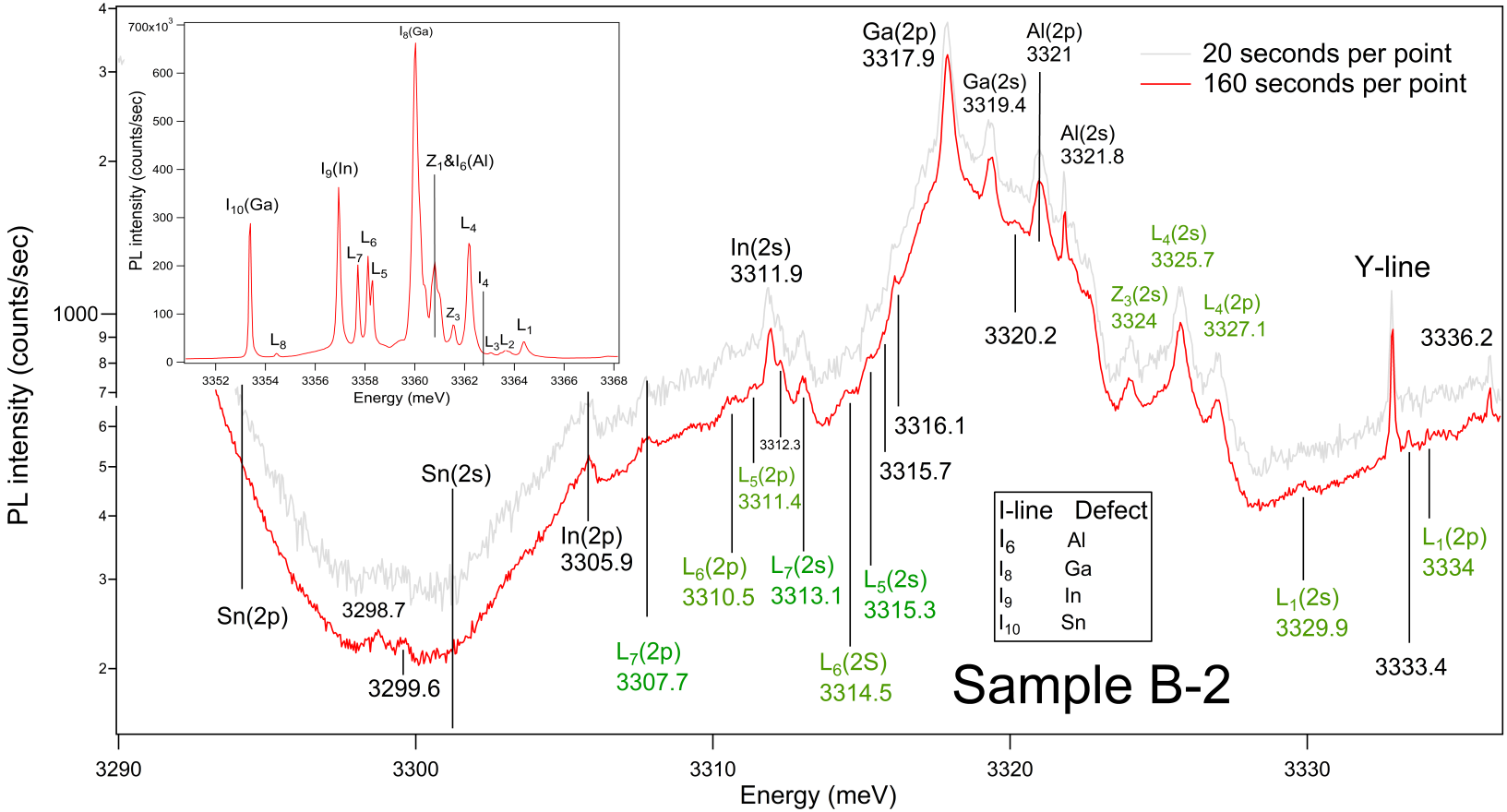

Figure 4.2: PL spectrum of the TES region for a sample showing strong L-lines. The impurities assigned to the I-lines are shown in the box. TES lines for the L-lines have been labeled based on how well they would fit in the linear relations for I-lines, i.e. how well they would follow the Haynes' rule, if they were assigned to a certain L-line. The numbers below the labels are the energy of the lines in meV. The lines that could not be assigned to a line in the exciton region are only labeled by their energy. The black lines crossing the plot demonstrate the expected position of the lines that did not show up in the PL spectrum. The positions are designated based on previous data [8] [7] Inset: PL result of the principal bound exciton region, i.e. 1s transition. I_4 has been labeled in the inset, the principal bound exciton region, not be confused with L_3 or L_4.

Table 4.1: Quantitative details for L-line and I-line positions and TES lines assigned to them.
[a] Based on reference [7]
[b] Based on reference [8]

Label	Localization energy (meV)	1s position (meV)	2s position (meV)	2p position (meV)	2s-1s separation (meV)	2s-1s separation prediction (meV)	2p-1s separation (meV)	2p-1s separation prediction (meV)	Donor binding energy (meV)
L_1	11.3	3364.4	3329.9	3334.0	34.5	33.8	30.4	29.6	43.0
L_2	12.0	3363.7	-	-	-	34.8	-	31.6	-
L_3	12.7	3363.0	-	-	-	35.9	-	33.6	-
L_4	13.5	3362.2	3325.7	3327.1	36.5	37.1	35.1	35.9	47.7
I_6	14.9	3360.8	3321.8	3321.0	39.0	39.2	39.9	39.9	52.5
I_8	15.7	3360.0	3319.4	3317.9	40.6	40.4	42.1	42.1	54.7
L_5	17.4	3358.3	3315.3	3311.4	43.0	42.9	46.9	47.0	59.5
L_6	17.6	3358.1	3314.5	3310.5	43.6	43.2	47.6	47.6	60.2
L_7	18.0	3357.7	3313.1	3307.7	44.6	43.8	50.0	48.7	62.6
I_9	18.8	3356.9	3311.9	3305.9	45.0	45.0	51.0	51.0	63.6
L_8	21.3	3354.4	-	-	-	48.8	-	58.1	-
I_{10}	22.3	3353.4	3405.5	$3413.6^a/3411.9^b$	52.1^b	50.3	$60.2^a/58.5^b$	61.0	$72.8^a/71.11^b$

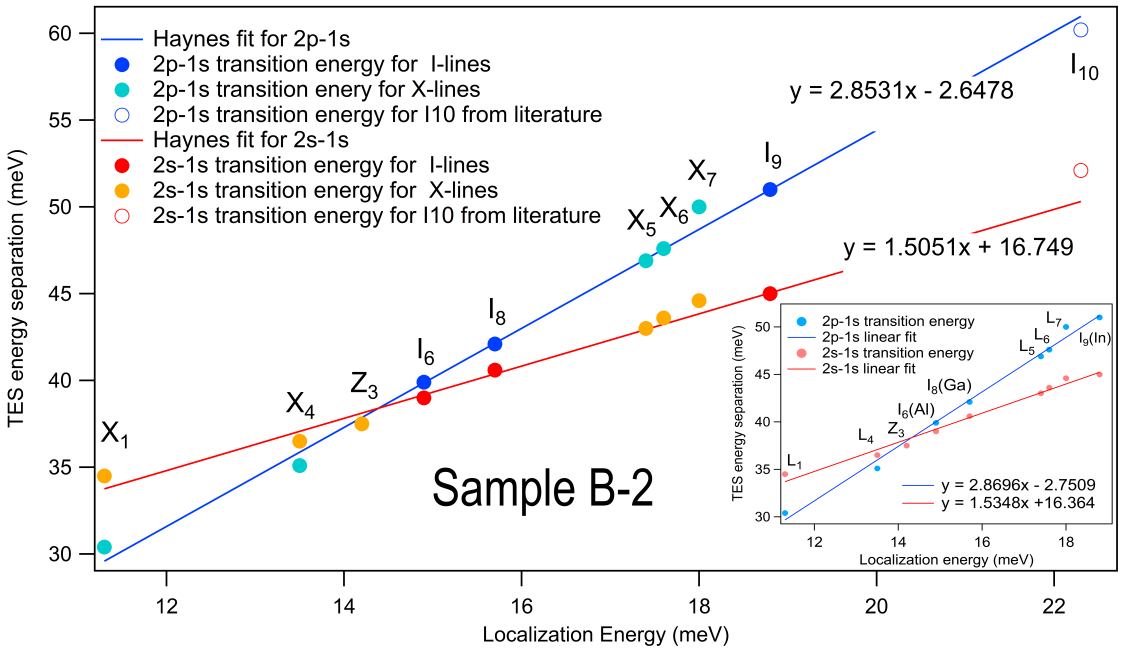

Figure 4.3: Plot of the TES lines positions vs. exciton localization energy for I-lines and L-lines in separate colors. Fit is to the three I-line data points. Inset:TES lines energy vs. exciton localization energy for I-lines and the L-lines. Fit was based on all points, including I, L and Z line data.

Fig 4.3 shows the location of the L-lines with respect to I-lines in the Haynes fit on I-lines. The labels for the I-lines and the fit to the TES lines for the I-lines are in a different color than the L-lines transitions. As shown in Fig 4.3, the L-lines agree with Haynes' rule very accurately, especially L_5 and L_6. The main plot shows a fit through the 3 I-lines. The inset shows a fit obtained on all I and L lines. The fitting parameters are quite similar. Small deviations of L-lines from the fitted line are observed and are likely due to differences in the core electron structure of a complex vs a substitutional group III impurity (I-lines). This is ample evidence showing that L-lines are due to donor bound excitons. However, further research is needed to determine the components of the impurities related to these lines.

For some of the lines the 2p-1s transition is below the 2s-1s, showing that the 2p level is below the 2s. As discussed in section 3.7.1 the discrepancy of TES lines energy locations from the EMA value is due to the central cell potential of the defects, which only affect the s orbitals. This short-range potential is usually negative resulting in the 2s level becoming deeper, while for defects at energies lower than the intersection of the fits in Fig. 4.3 it seems to be positive, resulting in a more shallow 2s level compared to the 2p orbital. We found the intersection of the two fits with more precision by fitting linear relations to all of the lines, including the I-lines and L-lines [see the inset of Fig. 4.3]. The intersection of the

lines at 14.32 meV for the localization energy and 38.34 meV for the TES energy separation shows where the 2p-1s and 2s-1s transitions have the same energy, hence where the 1p and 2s levels are equal. This means the central cell potential effect on the s orbitals is zero. Based on Eq. 1.7, The electron binding energy at that point would be around 50.9 meV which is in reasonable agreement with the theoretical value of 50.15 meV[7].

4.3 L-lines at higher energies

L_1, L_2, L_3 and L_4 are located at higher energies than the other L-lines. Lines at energies close to L_1-L_4 have been observed before. Previously observed lines I_4 and I_5, respectively at 3362.8 meV and 3361.4 meV [7], are close but do not align with any of the L-lines. Also, in CVD (chemical vapor deposition) samples grown on O-face ZnO substrates, lines labeled X_1, X_2, X_3 and X_4 have been found at 3361.85 meV, 3362.15 meV, 3363.65 meV and 3363.95 respectively [6]. X_2 seems to align with L_4 and X_3 with L_2, but it is not probable that they are the same lines. All the X-lines are attributed to the same defect for several reasons including the fact that they correlate in the ratio of their intensity. However in our case, L_2 and L_4 do not correlate in intensity. Also, there is no line in our samples that can be attributed to X_1 and X_4. In addition, the X-lines do not seem to be due to Li impurities. Among the possible candidates for the emergence of the X-lines a shallow donor consisted of Zn interstitial and an acceptor, most probably N_O, has been proposed[44]. We have shown evidence of new L-lines emerging alongside the I_{10} line. In section 3.6, I_{10} was shown to be Li related by means of lithium diffusion. This suggests that L-lines are Li related as well. Fig 3.8 shows the results of annealing under N_2 at temperatures of 450°C to 950°C on tin-doped ZnO samples. Annealing under N_2 gas might encourage the formation of N_O, which is speculated to be a component of the X-lines. None of those treatments have given rise to the L-lines. This suggests that L-lines are different from the X-lines. It is worth mentioning that the two lines on the right side of the I_6 in Fig. 3.8 are not L-lines but Z-lines, which are shallow donors bound to a complex of carbon and other unknown impurities [42]. Fig. 3.13 shows that also changing the environment from N_2-rich to O_2-rich does not give rise to the L-lines when there is no Li source used. This along with many other Li free treatments prove that Li has to do with the rise of the L-lines either as a component or as a means of formation of the defects.

Looking at the principal bound exciton region it is evident that L_2, L_3 and Z_3 are very weak compared to the other lines, therefore its no surprise that the corresponding TES lines do not appear in the TES region. Equivalent TES lines for L_2, L_3 and Z_3 are expected to be almost proportionally weak compared to the other TES lines as their BX lines are. As a result, they would not appear in the TES region in an intensity greater than the noise spikes. Therefore the unknown TES lines in the area where L_1-L_4 TES line are expected to

be were confidently assigned to only L_1 and L_4.

Another reason for the TES lines of the L_2 and L_3 not being observed in the TES region could be that they are D^+X lines rather than D^0X. A D^+X does not have TES lines since after they recombine there is no electron on the outer shell of the donor that could end up in an excited state. L_2 and L_3 appear at higher energies compared to most of the I-lines and L-lines where D^+X lines are more likely to be, which further suggests investigating if they are D^+X. The reason for the emergence of D^+X after the Li diffusion could be the excess concentration of Li acceptors that removes the electron from the donors as a result of compensation.

I_6, I_8 and I_9 are known to have their corresponding D^+X lines at higher energies. The

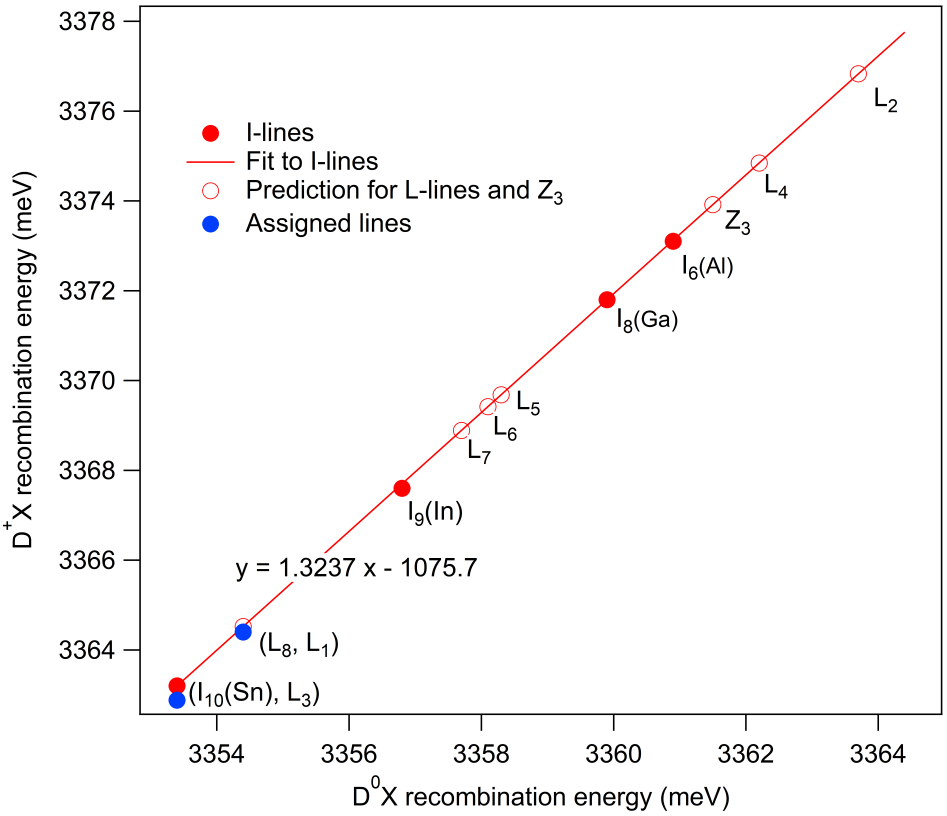

Figure 4.4: Plot of the energy location of D^+X versus 1s D^0X.

D^+X energies for I_6, I_8, I_9 and I_{10} are respectively 3373.1 [8] 3371.8 meV and 3367.6 meV [7] and 3363.2[27][45]. The location of ionized bound exciton of I_{10} is very close to L_3 at 3363.0 meV. This suggests that L_3 could be the D^+X of the I_{10}.

To investigate whether any of the new L-lines can be the D^+X of the other L-lines we predict the location of their D^0X. Again, based on Haynes' rule, the 1s energy location of

the D^0X versus the energy location of D^+X for different lines will have a linear relation. Fig 4.4 shows a linear fit for I_6, I_8, I_9 and I_{10}. having the 1s locations of the L-lines we can predict the D^+X location of them. The results show that the prediction for the D^+X of L_8 would be 3364.5 meV which is close to the location of L_1 at 3364.4. We can hardly assign L_1 to the D^+X of L_8 in that the TES lines for the L_1 has been found which means it cannot be a D^+X as discussed before. In addition, L_8 is a very weak line. Usually, D^+X lines are accompanied by strong corresponding D^0X lines.

L_1 seems to arise only as a result of Li diffusion under N_2 and is eliminated by an O_2-rich

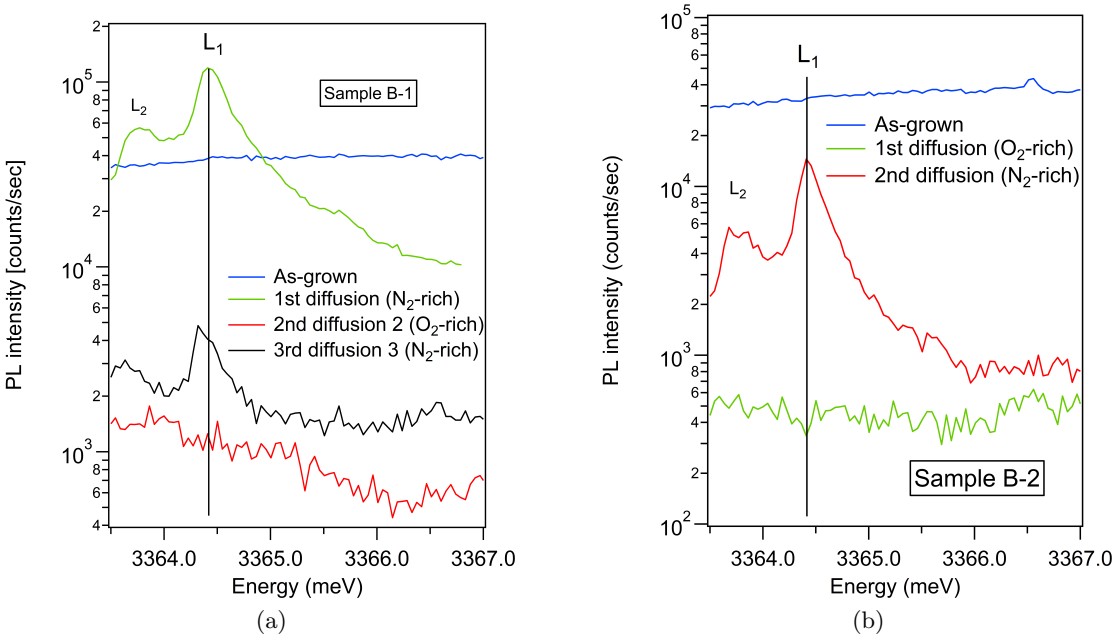

Figure 4.5: Effect of successive lithium diffusion in Sn-doped bulk ZnO samples on L_1 intensity. It is important to notice that all of the plots in each figure are from one sample. a) The original sample was treated under N_2-rich, then O_2-rich and then again N_2-rich environment respectively. b) The original sample was treated under O_2-rich and then N_2-rich respectively.

treatment. In Fig 4.5(a) the first treatment under N_2 gives rise to L_1, while in Fig 4.5(b) an O_2-rich treatment does not. It is worth noting that both of the first treatments are done on the as-grown sample. The second treatment in Fig 4.5(a), which is under O_2, shows the elimination of the L_1 peak that emerged in the first treatment. On the other hand, the second treatment in Fig 4.5(b) shows an increase in L_1, as expected. The third treatment in Fig 4.5.a also agrees with the trend, i.e it results in an increase in L_1. This suggests that there is a component in this defect that is enhanced by N_2 and removed by O_2. A more probable explanation is that an O_2-rich treatment turns L_1 to another defect by adding an extra element to the impurity rather than removing the element added by the N_2-rich treatment. We know that an O_2-rich environment encourages Zn-vacancies as the O_2 molecules

react with interstitial Zn on the surface to form ZnO. This reduces the concentration of the Zn interstitial and pushes it out of equilibrium. Therefore Zn vacancies are formed to produce more Zn interstitial.

Among all the L-lines, L-L_1 seems to be the shallowest line appearing at 3360.0 meV. This is more shallow than the hydrogen-related I_4[7] which used to be known as the shallowest D^0X. But in 2013 a new line found in Sb doped nanowire samples was found at 3364.3 meV which is shallower than L_1 and still the shallowest [24].

4.4 L-lines at lower energies

L_5, L_6 and L_7 seem to only increase with Li diffusion only if there are previous signs of those lines in the spectrum before the treatment. In contrast, L_1-L_3 and L_8 can emerge in samples that do not show them prior to the Li diffusion. This can be seen in Fig. 4.1 as well as the results of many other Li diffusion experiments. This suggests that L_5, L_6 and L_7 might consist of some kind of unexpected residual impurity involved in the defect that only exists in some of our samples. Therefore, the result of Li-diffusion in samples that do not have those impurities will not show the L-lines even after Li diffusion. Fig. 4.6 shows the result of Li diffusion at 450°C where L_5, L_6 and L_7 emerged neither before nor after the diffusion, while other L-lines seem to emerge although they did not exist in the spectrum prior to the Li diffusion. Among the expected defects are native defects[33] and the elements assigned to the I-lines including Al, Ga, In, Sn and especially Li which has been intentionally doped into the samples. L_4 sits in a gray area where it shows some spikes before Li diffusion but those spikes cannot clearly be distinguished from noise spikes.

L_8 seems to be susceptible to the environment in which Li diffusion has happened. It only arises as a result of Li diffusion under N_2, but unlike L_1 is not eliminated after an O_2-rich treatment. As in Fig 4.7(a) the first treatment under N_2 gives rise to X_8, while in Fig 4.7(b) similar O_2-rich treatment does not. The second treatment in Fig 4.7.a, under O_2, shows a negligible change in L_8. The second treatment in Fig 4.7(b) shows an increase in L_8, as expected. The third treatment in Fig 4.7(a) also agrees with the trend i.e negligible change in L_8. Since O_2 does not eliminate L_8 the most probable speculation about the origin of this line is that it is due to a defect that consists of a component created by N_2 treatment but not by O_2. Also, there might be a component to this defect that is removed by N_2 that transforms a defect to L_8 while it is not removed by O_2. A Zn-vacancy is such a component. It is worth mentioning that L_8 was comparatively weak and similar to L_2 and L_3 did not appear in the TES region.

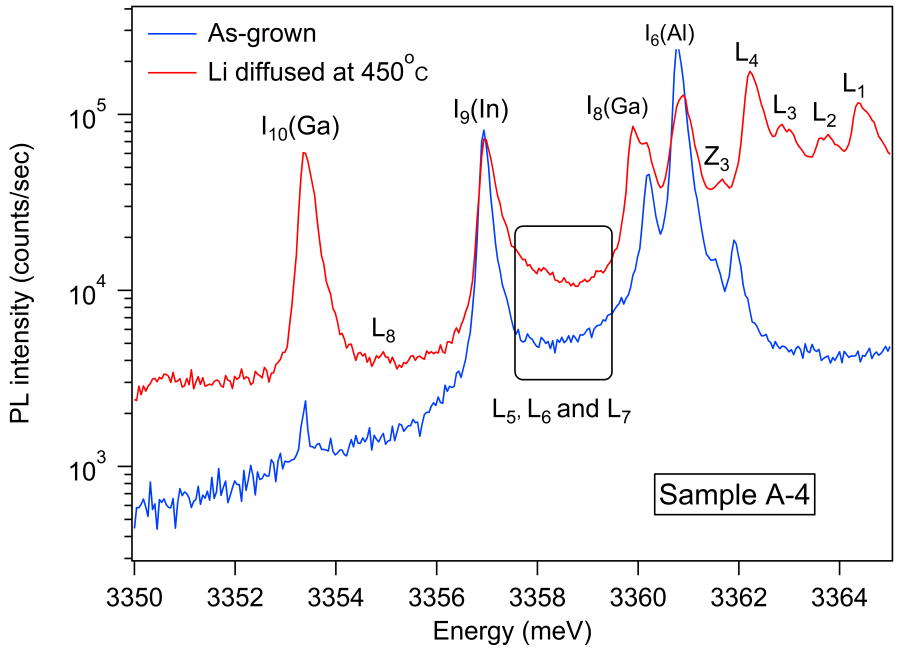

Figure 4.6: The result of Li diffusion at 450°C on a sample with no previous sign of L_5, L_6 and L_7. All the L-lines except L_5, L_6 and L_7 have arisen as expected.

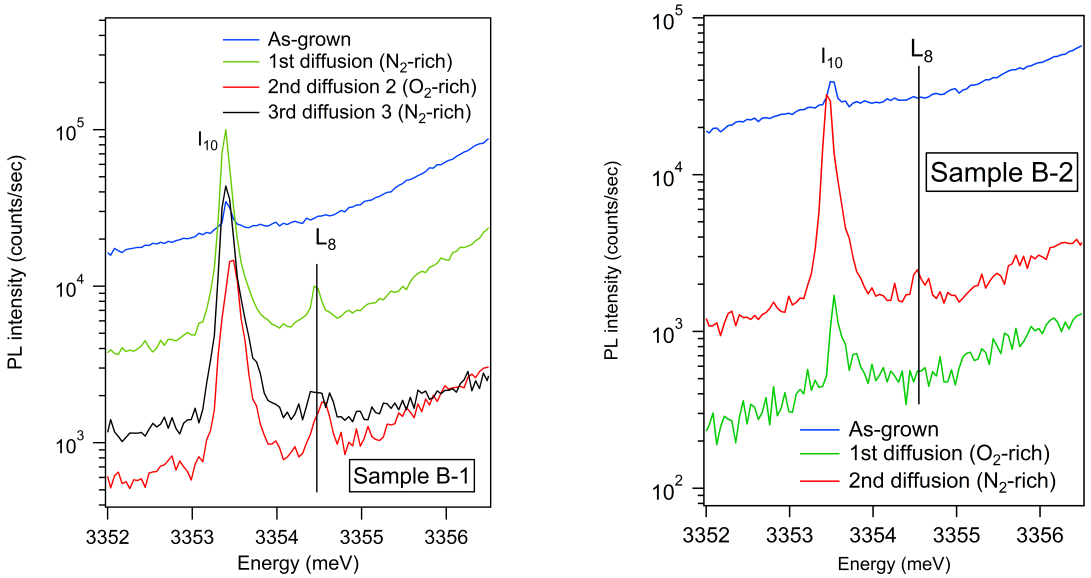

Figure 4.7: Effect of successive lithium diffusion in Sn-doped bulk ZnO samples on L_8 intensity. It is important to notice that all of the plots in each figure are from one sample. a) The original sample was treated under N_2-rich, then O_2-rich and then again N_2-rich environment respectively. b) The original sample was treated under O_2-rich and then N_2-rich respectively.

Chapter 5

Conclusion

We have investigated several lithium-related defects in ZnO by high-resolution PL spectroscopy at low temperature. Li diffusion in O-rich (under O_2 gas) and Zn-rich (under N_2 gas) conditions was implemented to investigate the relation between the optical properties of the samples and the Li content of the sample.

The I_{10} line, previously known to be due to a defect containing Sn impurities, at 3353.4 meV was proven in this work to be a Sn+Li complex. Annealing the sample at temperatures from 450°C to 900°C in Zn-rich conditions shows a reduction in the intensity of I_{10} with thermally activated diffusion of Li out of the sample. The rate of removal of Li shows an activation energy of E_d= 0.4 eV ± 0.2eV for the removal of Li from the defect. This activation energy shows a large discrepancy from what we theoretically expected from our hypothesis for the simplest structural model of the defect. Our hypothesis was a defect consisting of Sn and Li at the nearest neighboring Zn sites in ZnO. Previous theoretical values of the formation energies derived from DFT calculation were used to estimate the energy of removal of the Li form the defect. The calculated values were based on two mechanisms for the removal of Li from the complex. Based on the dissociation mechanism the Li impurity is dissociated from the defect and occupies an interstitial site leaving a Zn-vacancy at the defect and then diffuses further away from the remaining defect in an interstitial form. This mechanism should give a value of 3.5 eV for Zn-rich diffusion condition. The other mechanism is based on a kick-out process where the Li in the defect is kicked out by an interstitial Zn and the Zn is substituted at the position of Li, i.e. a Zn site. We derived a value of 4.8 eV for the activation energy of this mechanism based on previous DFT calculations. This discrepancy suggests that the I_{10} defect is more complicated than the hypothesis. We repeated this experiment this time under O_2. The results were significantly different. It seemed like there is no diffusion of Li out of the sample under 800 °C. After 800°C a sudden drop was observed, which shows the out-diffusion of Li_{Zn}.

The diffusion of Li into the sample from a coating of lithium carbonate at between 450°C

and 900°C returned the I_{10} to an intensity comparable with the initial intensity ratio. Also, the diffusion of Li into many other samples shows a correlation between the Li concentration in the sample and the intensity of I_{10}. This is strong evidence that confirms the involvement of a Li component in the formation of the I_{10} defect.

To further investigate the existence of Li in the I_{10} we investigated whether the position of the I_{10} changes with the isotope of the Li. We used a model by Heine et al. to theoretically estimate the shift we expect from the substitution of natural Li with ^{6}Li. Based on the model, a shift of less than 0.031 meV toward the higher energies is expected. Our experimental results were in a reasonable agreement with that value, showing an average shift of 0.012 meV toward the higher energies, or 0.022 meV after removing one of the data points that we attribute as an outlier. We do not expect to see signs of line splitting in I_{10} as the linewidth is much larger than the expected splitting. The number of data points being only three among which we observed of an outlier casts a shadow on the reliability of the results. More investigation, with a higher number of experiments and data points, as well as higher resolution spectroscopy is needed to confirm the results. Other techniques such as electron paramagnetic resonance, which are sensitive to nuclear spin would be able to clarify the role of Li in these defects.

Besides an increase in I_{10}, we observed the rise of new lines and an increase in the intensity of many unidentified lines as a result of Li diffusion. We called them L-lines and labeled them from L_1 to L_8. We confirmed they are all bound exciton lines by investigating whether they follow the Haynes' rule for bound excitons. We showed that the exciton localization energy and the 2p-1s separation of the lines, therefore the donor binding energies, show a highly linear relation. This is strong evidence for the excitonic origin of the lines. We were also able to assign L_3 to the D^+X of I_{10}. Some detailed properties of the lines were discussed based on multiple Li diffusion experiments with varying environment between O-rich and Zn-rich conditions.

I_{10} is under consideration as a potential donor for quantum information applications. We have shown that the concentration of this defect can be controlled by the addition of Li. A Low concentration of Li results in very narrow linewidth of I_{10}, which makes it useful for our collaborators[46]. The ability to control the defect concentration by thermal annealing offers a way to achieve low concentrations.

Bibliography

[1] Klaus Ellmer and Andreas Klein. ZnO and its applications. In *Transparent conductive zinc oxide*, pages 1–33. Springer, 2008.

[2] D. G. Thomas. The exciton spectrum of zinc oxide. *Journal of Physics and Chemistry of Solids*, 15(1-2):86–96, 1960.

[3] C. Merz, M. Kunzer, U. Kaufmann, I. Akasaki, and H. Amano. Free and bound excitons in thin wurtzite GaN layers on sapphire. *Semiconductor Science and Technology*, 11(5):712, 1996.

[4] Xiayu Linpeng, Maria L. K. Viitaniemi, Aswin Vishnuradhan, Y. Kozuka, Cameron Johnson, M. Kawasaki, and Kai-Mei C. Fu. Coherence properties of shallow donor qubits in ZnO. *Physical Review Applied*, 10(6):064061, 2018.

[5] G. Dresselhaus. Effective mass approximation for excitons. *Journal of Physics and Chemistry of Solids*, 1(1-2):14–22, 1956.

[6] Markus R. Wagner, Til P. Bartel, Ronny Kirste, Axel Hoffmann, Joachim Sann, Stefan Lautenschläger, Bruno K. Meyer, and C. Kisielowski. Influence of substrate surface polarity on homoepitaxial growth of ZnO layers by chemical vapor deposition. *Physical Review B*, 79(3):035307, 2009.

[7] B. K. Meyer, H. Alves, 1, D. M. Hofmann, W. Kriegseis, D. Forster, F. Bertram, J. Christen, A. Hoffmann, M. Straßburg, M. Dworzak, et al. Bound exciton and donor–acceptor pair recombinations in ZnO. *physica status solidi (b)*, 241(2):231–260, 2004.

[8] Faezeh Mohammadbeigi. *Optical Characterization of Doped Zinc Oxide Nanowires*. PhD thesis, Simon Fraser University, 2017.

[9] Ü. mit Özgür, Ya. I. Alivov, C.hunli Liu, A. Teke, M. A.n Reshchikov, S. Doğan, V.CSJ Avrutin, S.-J. Cho, Morkoç, and H. A comprehensive review of ZnO materials and devices. *Journal of Applied Physics*, 98(4):11, 2005.

[10] D. C. Reynolds, C. W. Litton, and T. C. Collins. Zeeman effects in the edge emission and absorption of ZnO. *Physical Review*, 140(5A):A1726, 1965.

[11] David C. Look, D. C. Reynolds, C. W. Litton, R. L. Jones, D. B. Eason, and G. Cantwell. Characterization of homoepitaxial p-type ZnO grown by molecular beam epitaxy. *Applied Physics Letters*, 81(10):1830–1832, 2002.

[12] Atsushi Tsukazaki, Akira Ohtomo, Takeyoshi Onuma, Makoto Ohtani, Takayuki Makino, Masatomo Sumiya, Keita Ohtani, Shigefusa F Chichibu, Syunrou Fuke, Yusaburou Segawa, et al. Repeated temperature modulation epitaxy for p-type doping and light-emitting diode based on ZnO. *Nature Materials*, 4(1):42–46, 2005.

[13] E. Przeździecka, E. Kamińska, I. Pasternak, A. Piotrowska, and J. Kossut. Photoluminescence study of p-type ZnO: Sb prepared by thermal oxidation of the Zn-Sb starting material. *Physical Review B*, 76(19):193303, 2007.

[14] J. R. Haynes. Experimental proof of the existence of a new electronic complex in silicon. *Physical Review Letters*, 4(7):361, 1960.

[15] Pierre Hohenberg and Walter Kohn. Inhomogeneous electron gas. *Physical Review*, 136(3B):B864, 1964.

[16] Walter Kohn and Lu Jeu Sham. Self-consistent equations including exchange and correlation effects. *Physical Review*, 140(4A):A1133, 1965.

[17] Ymir Kalmann Frodason. Zinc vacancy–donor defect complexes in crystalline zinc oxide: A hybrid density functional study. Master's thesis, University of Oslo, 2016.

[18] N. M. Harrison. An introduction to density functional theory. *Nato Science Series Sub Series III Computer and Systems Sciences*, 187:45–70, 2003.

[19] Fumiyasu Oba, Minseok Choi, Atsushi Togo, and Isao Tanaka. Point defects in ZnO: an approach from first principles. *Science and Technology of Advanced Materials*, 12(3):034302, 2011.

[20] Christoph Freysoldt, Blazej Grabowski, Tilmann Hickel, Jörg Neugebauer, Georg Kresse, Anderson Janotti, and Chris G. Van de Walle. First-principles calculations for point defects in solids. *Reviews of Modern Physics*, 86(1):253, 2014.

[21] V. Heine and C. H. Henry. Theory of the isotope shift for zero-phonon optical transitions at traps in semiconductors. *Physical Review B*, 11(10):3795, 1975.

[22] Y. Yu Peter and Manuel Cardona. Temperature coefficient of the refractive index of diamond-and zinc-blende-type semiconductors. *Physical Review B*, 2(8):3193, 1970.

[23] T. N. Morgan, B. Welber, and R. N. Bhargava. Optical properties of Cd-O and Zn-O complexes in GaP. *Physical Review*, 166(3):751, 1968.

[24] E. Senthil Kumar, F. Mohammadbeigi, S. Alagha, Z. W. Deng, I. P. Anderson, T. Wintschel, and S. P. Watkins. Optical evidence for donor behavior of Sb in ZnO nanowires. *Applied Physics Letters*, 102(13):132105, 2013.

[25] J. A. Sans, A. Segura, M. Mollar, and B. Marı. Optical properties of thin films of ZnO prepared by pulsed laser deposition. *Thin Solid Films*, 453:251–255, 2004.

[26] Joseph Cullen, Daragh Byrne, K. Johnston, Enda McGlynn, and Martin O. Henry. Chemical identification of luminescence due to Sn and Sb in ZnO. *Applied Physics Letters*, 102(19):192110, 2013.

[27] E. Senthil Kumar, F. Mohammadbeigi, Lynn A. Boatner, and S. P. Watkins. High-resolution photoluminescence spectroscopy of Sn-doped ZnO single crystals. *Journal of Luminescence*, 176:47–51, 2016.

[28] E. Tomzig and R. Helbig. Band-edge emission in ZnO. *Journal of Luminescence*, 14(3):403–415, 1976.

[29] R. Marquez and C. Rincón. Defect physics of ternary chalcopyrite semiconductors. *Materials Letters*, 40(2):66–70, 1999.

[30] Thomas Neset Sky, K. M. Johansen, Ymir Kalmann Frodason, Bengt Gunnar Svensson, and Lasse Vines. The interaction between lithium acceptors and gallium donors in zinc oxide. *Journal of Applied Physics*, 124(24):245702, 2018.

[31] A. Carvalho, Audrius Alkauskas, Alfredo Pasquarello, A. K. Tagantsev, and N. Setter. A hybrid density functional study of lithium in ZnO: Stability, ionization levels, and diffusion. *Physical Review B*, 80(19):195205, 2009.

[32] We T. Hicks. Evaluation of vapor-pressure data for mercury, lithium, sodium, and potassium. *The Journal of Chemical Physics*, 38(8):1873–1880, 1963.

[33] Anderson Janotti and Chris G. Van de Walle. Native point defects in ZnO. *Physical Review B*, 76(16):165202, 2007.

[34] SL Chen, WM Chen, and IA Buyanova. Dynamics of donor bound excitons in zno. *Applied Physics Letters*, 102(12):121103, 2013.

[35] J. J. Lander. Reactions of lithium as a donor and an acceptor in ZnO. *Journal of Physics and Chemistry of Solids*, 15(3-4):324–334, 1960.

[36] P. Dahan, V. Fleurov, P. Thurian, R. Heitz, A. Hoffmann, and I. Broser. Isotope shift in semiconductors with transition-metal impurities: Experiment and theory applied to ZnO: Cu. *Physical Review B*, 57(16):9690, 1998.

[37] Koichi Momma and Fujio Izumi. Vesta: a three-dimensional visualization system for electronic and structural analysis. *Journal of Applied Crystallography*, 41(3):653–658, 2008.

[38] R. C. Rai, M. Guminiak, S. Wilser, B. Cai, and M. L. Nakarmi. Elevated temperature dependence of energy band gap of ZnO thin films grown by e-beam deposition. *Journal of Applied Physics*, 111(7):073511, 2012.

[39] William N. Lawless and Tapan K. Gupta. Thermal properties of pure and varistor ZnO at low temperatures. *Journal of Applied Physics*, 60(2):607–611, 1986.

[40] A. Yang, M. Steger, T. Sekiguchi, D. Karaiskaj, M. L. W. Thewalt, M. Cardona, Kohei M. Itoh, H. Riemann, N. V. Abrosimov, M. F. Churbanov, et al. Single-frequency laser spectroscopy of the boron bound exciton in ^{28}Si. *Physical Review B*, 80(19):195203, 2009.

[41] P. J. Dean, C. J. Frosch, and C. H. Henry. Optical properties of the group IV elements carbon and silicon in gallium phosphide. *Journal of Applied Physics*, 39(12):5631–5646, 1968.

[42] Faezeh Mohammadbeigi. *Optical characterization of doped zinc oxide nanowires*. PhD thesis, Science: Department of Physics, 2017.

[43] A. V. Rodina, M. Dietrich, A. Göldner, L. Eckey, A. Hoffmann, Al L. Efros, M. Rosen, and B. K. Meyer. Free excitons in wurtzite GaN. *Physical Review B*, 64(11):115204, 2001.

[44] David C. Look, Gary C. Farlow, Pakpoom Reunchan, Sukit Limpijumnong, S. B. Zhang, and Kai Nordlund. Evidence for native-defect donors in n-type ZnO. *Physical Review Letters*, 95(22):225502, 2005.

[45] B. K. Meyer, J. Sann, S. Lautenschläger, M. R. Wagner, and A. Hoffmann. Ionized and neutral donor-bound excitons in ZnO. *Physical Review B*, 76(18):184120, 2007.

[46] Xiayu Linpeng, Todd Karin, M. V. Durnev, Russell Barbour, M. M. Glazov, E. Ya Sherman, S. P. Watkins, Satoru Seto, and Kai-Mei C. Fu. Longitudinal spin relaxation of donor-bound electrons in direct band-gap semiconductors. *Physical Review B*, 94(12):125401, 2016.

Appendix A

Table of samples and treatment

Table A.1: Table of sample labels and treatments performed on them. Samples with the same alphabet in their labels are from the same growth.
[a]This sample is the same sample as B-1. The double labeling is for aesthetics of Fig. 3.19

Sample Label	Shape	Treatment type	Temperature (°C)	Condition	PL figure
A-1	Bulk	Annealing	450-950	N_2-rich	Fig 3.8
		Natural Li diffusion	450	N_2-rich	Fig 3.15
A-2	Bulk	Annealing	400-900	N_2-rich	Fig 3.13
A-3	Bulk	Natural Li diffusion	450	N_2-rich	Fig 3.16
		Natural Li diffusion	550	N_2-rich	Fig 3.16
A-4	Bulk	Natural Li diffusion	450	N_2-rich	Fig 4.6
B-1	Needle	Natural Li diffusion	450	N_2-rich	Fig 4.5.a, Fig 4.7.a
		Natural Li diffusion	450	O_2-rich	Fig 4.5.a, Fig 4.7.a
		Natural Li diffusion	450	N_2-rich	Fig 4.5.a, Fig 4.7.a, Fig. 4.1, Fig. 3.16
B-2	Needle	Natural Li diffusion	450	O_2-rich	Fig 4.5.b, Fig 4.7.b
		Natural Li diffusion	450	N_2-rich	Fig 4.5.b, Fig 4.7.b, Fig 4.2
SN-1	Needle	Natural Li diffusion	950	N_2-rich	Fig. 3.19
SN-2	Needle	Natural Li diffusion	950	N_2-rich	Fig. 3.19
SN-3	Needle	Natural Li diffusion	950	N_2-rich	Fig. 3.19
S6-1	Needle	^{6}Li diffusion	450	N_2-rich	Fig. 3.19
S6-2[a]	Needle	^{6}Li diffusion	450	N_2-rich	Fig. 3.19
S6-3	Needle	^{6}Li diffusion	450	N_2-rich	Fig. 3.19
N-1	Nanowires	No treatment	NA	NA	Fig. 2.3
N-2	Nanowires	Grown in Li contaminated chamber	NA	NA	Fig. 2.3
N-3	Nanowires	No treatment	NA	NA	Fig. 2.3
N-4	Nanowires	Natural Li diffusion	450	N_2-rich	Fig. 3.19
N-5	Nanowires	Natural Li diffusion	450	N_2-rich	Fig. 3.19
N-6	Nanowires	Natural Li diffusion	450	N_2-rich	Fig. 3.19
N-7	Nanowires	Natural Li diffusion	450	N_2-rich	Fig. 3.19